

# Meningioma Analysis and Diagnosis using Limited Labeled Samples

Jiamiao Lu<sup>a,1</sup>, Wei Wu<sup>b,1</sup>, Ke Gao<sup>b</sup>, Ping Mao<sup>b</sup>, Weichuan Zhang<sup>a,\*</sup>, Tuo Wang<sup>b,\*</sup>, Lingkun Ma<sup>a,\*</sup>, Jiapan Guo<sup>d,\*</sup>, Zanyi Wu<sup>c,\*</sup>, Yuqing Hu<sup>e</sup> and Changming Sun<sup>f</sup>

<sup>a</sup>*Shaanxi University of Science and Technology, Xi'an, Shaanxi, China*

<sup>b</sup>*Department of Neurosurgery, The First Affiliated Hospital of Xi'an Jiaotong University, Xi'an, Shaanxi, 710061, China*

<sup>c</sup>*Department of Neurosurgery, The First Affiliated Hospital of Fujian Medical University, Fuzhou, Fujian, China*

<sup>d</sup>*Department of Radiotherapy, University of Groningen, University Medical Center Groningen, Groningen, The Netherlands*

<sup>e</sup>*Department of Nephrology, Chenggong Hospital Affiliated to Xiamen University, Xiamen, Fujian, China*

<sup>f</sup>*CSIRO Data61, Epping, NSW, Australia*

## ARTICLE INFO

### Keywords:

Meningiomas  
discrete wavelet transform  
few-shot learning  
self-supervised scale and affine invariant network

## ABSTRACT

The biological behavior and treatment response of meningiomas depend on their grade, making an accurate diagnosis essential for treatment planning and prognosis assessment. We observed that the weighted fusion of spatial-frequency domain features significantly influences meningioma classification performance. Notably, the contribution of specific frequency bands obtained by discrete wavelet transform varies considerably across different images. A feature fusion architecture with adaptive weights of different frequency band information and spatial domain information is proposed for few-shot meningioma learning. To verify the effectiveness of the proposed method, a new MRI dataset of meningiomas is introduced. The experimental results demonstrate the superiority of the proposed method compared with existing state-of-the-art methods in three datasets. The code will be available at: <https://github.com/ICL-SUST/AMSF-Net>.

## 1. Introduction

Meningiomas, originating from arachnoid cap cells, represent the most common primary central nervous system tumor, accounting for approximately 37.6% of all such neoplasms and exhibiting a global incidence rate of around 8.83 per 100,000 individuals, with increasing prevalence in aging populations [125, 100]. These tumors display a wide spectrum of biological behaviors, influenced by their histological grade as defined by the World Health Organization (WHO) [129, 126, 37]: benign (grade I, ~80%), atypical (grade II, ~17.7%), and malignant (grade III, ~1.7%), each associated with distinct risks of invasiveness and response to therapy [125]. Globally, these tumors impose significant healthcare burdens, particularly in females and older adults, where advanced imaging modalities like magnetic resonance imaging (MRI) are essential for initial assessment [125, 100]. MRI sequences, such as T1-weighted contrast-enhanced (T1CE), T2-weighted, and fluid-attenuated inversion recovery (FLAIR), offer insights into tumor morphology, edema, and enhancement patterns [58, 119]. However, histopathological examination post-resection remains the gold standard for definitive grading, supplemented by molecular markers like TERT promoter mutations or CDKN2A/B deletions in the latest WHO CNS5 updates [115, 105, 36, 121]. Despite these tools, traditional diagnostics face challenges: histopathological sampling bias fails to capture

intratumoral heterogeneity, while MRI often lacks precision in predicting aggressive behavior non-invasively, due to limitations in feature validation, small sample sizes, and subjective interpretation [81, 96, 119].

The integration of artificial intelligence (AI) has revolutionized medical imaging by enabling the automated extraction of features and recognition of patterns [23, 11]. Traditional machine learning methods, including support vector machines (SVM) and random forests (RF), have been applied to radiomic features from multi-sequence MRI, achieving high area under the curve (AUC) values for distinguishing high- from low-grade meningiomas [96, 135]. Deep learning models, such as convolutional neural networks (CNNs) [24] and vision transformers (ViTs) [4, 110], further advance performance by learning hierarchical representations directly from images [64, 111]. Recent reviews highlight AI's role in identifying novel radiological biomarkers for meningioma detection, grading, and segmentation, with meta-analyses showing promising diagnostic accuracy in deep learning applications [87, 96, 135]. These advancements support personalized medicine, reducing the need for invasive procedures and optimizing clinical workflows [23, 11].

Despite these progresses, key gaps remain in meningioma diagnostics [125]. Histopathological grading is invasive and susceptible to sampling errors, while imaging-based approaches face data scarcity due to high MRI costs, privacy concerns, and rare subtypes, often resulting in overfitting and limited generalization [81, 56, 98, 59]. CNNs [33, 24] excel in local feature extraction but are limited by inductive biases that impair long-range dependency capture, essential for delineating tumor boundaries and edema [65, 5]. Vision transformers provide global context but perform sub-optimally in fine-grained local features [5, 111]. Few-shot

\*Corresponding authors.

✉ 241612058@sust.edu.cn (J. Lu); 576223193@qq.com (W. Wu); 285640539@qq.com (K. Gao); mp10101@sina.com (P. Mao); zwc2003@163.com (W. Zhang); wt1972@tom.com (T. Wang); malingkun@sust.edu.cn (L. Ma); j.guo@umcg.nl (J. Guo); kirby98@126.com (Z. Wu); ahkong23@sina.com (Y. Hu); changming.sun@csiro.au (C. Sun)

ORCID(s):

<sup>1</sup>These authors contributed equally.

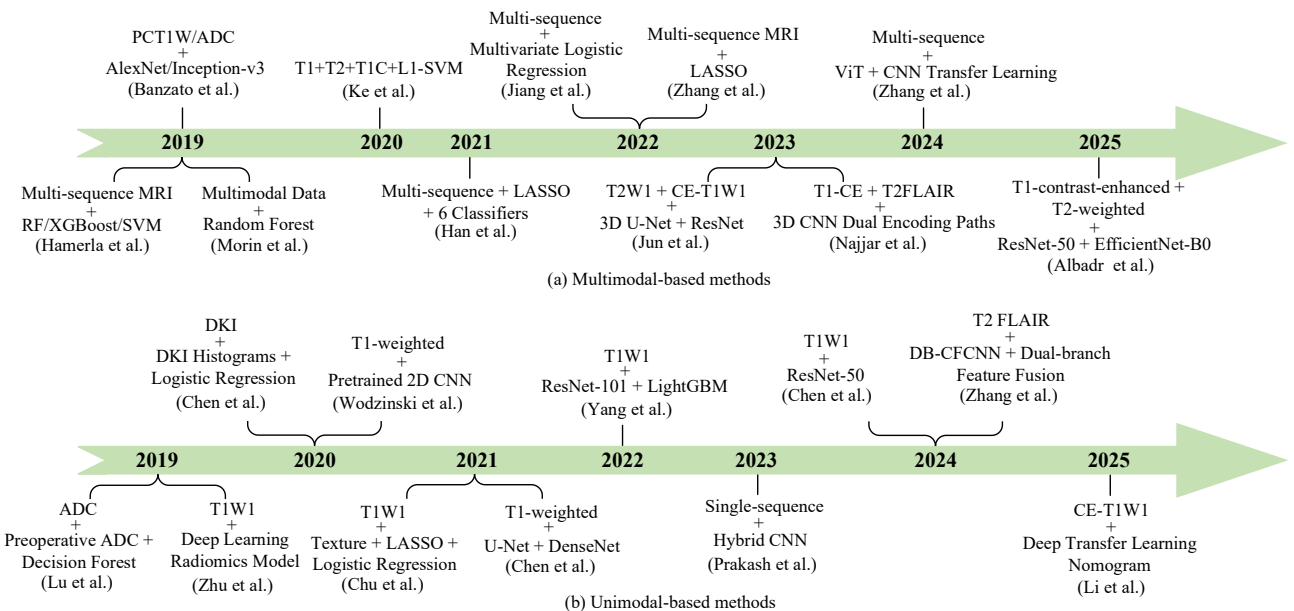


**Figure 1:** Timeline of the development of meningioma diagnosis and grading techniques. (a) Multimodal-based methods; (b) Unimodal-based methods.

learning has emerged to address data limitations, yet its integration with multi-resolution analysis, such as frequency-domain processing, is underexplored in meningioma diagnosis and grading [92, 96, 119].

This study addresses these gaps through a comprehensive review of AI-driven methods for meningioma diagnosis and grading, emphasizing traditional machine learning and deep learning applications. We observed that the weighted fusion of spatial-frequency domain features significantly influences meningioma classification performance. Notably, the contribution of specific frequency bands obtained by the discrete wavelet transform varies considerably across different images. Then we propose an adaptive feature fusion architecture integrating spatial and frequency-domain information with a vision transformer backbone for few-shot meningioma learning. To verify the effectiveness of the proposed method, a new MRI dataset of meningiomas (i.e., XJTU Meningioma dataset) is introduced. The experimental results demonstrate the superiority of the proposed method compared with existing state-of-the-art methods in three datasets.

## 2. Related Work

In this section, existing diagnosis and grading of meningiomas methods are systematically reviewed which can be classified into two groups [125, 108]: multimodal-based and unimodal-based methods as shown in Fig. 1. Multimodal methods integrate diverse data types, including multi-sequence MRI, imaging-derived features (e.g., radiomics and deep-learning representations), and non-imaging data (e.g., clinical and biomarker information), for enhancing

diagnostic accuracy by leveraging complementary information across these domains [76, 159, 9]. In contrast, unimodal methods [119, 108, 90] rely on a single imaging source, offering benefits such as simpler acquisition, less complex modeling, and reduced computational demands [82, 49, 122].

### 2.1. Multimodal-based Methods

Multimodal-based methods aim to improve meningioma grading accuracy by integrating complementary information from multiple MRI sequences and clinical data. In the work of [89], an integrated prognostic model was introduced which combines clinical variables, radiological semantic features, and radiomic features to grading prediction and uncover associations with molecular markers [63, 3, 102]. To mitigate sampling bias arising from manual region of interest (ROI) selection [89], Li et al. [67] applied 3D whole-tumor histogram analysis [88, 43] combined with logistic regression. This method involved comprehensive volumetric assessment using conventional MRI data from 90 patients.

As foundational radiomics methods have advanced, subsequent research has emphasized advanced feature extraction and selection to boost generalizability across institutions. Ke et al. [54] integrated texture and radiological features from multi-sequence MRI in 263 patients, achieving robust performance over single-sequence methods, though limited by data from only two centers. To enhance applicability, Laukamp et al. [61] demonstrated the transferability of radiomics-based grading across heterogeneous, multi-institutional MRI datasets, supporting its feasibility in diverse scanners and protocols. Building on these integrations, multimodal strategies have increasingly targeted finer-grained tasks, such as distinguishing tumor grades and histologic subtypes. Dorfner et al. [26] and LaBella

et al. [60] collectively explored multiparametric MRI with SVM and RF classifiers for grade and subtype differentiation; however, small cohort sizes limited generalizability. To overcome sample size limitations, we used large cohorts and applied LASSO based feature selection followed by RF classification [102, 72, 77, 160]. Furthermore, Han et al. [39] advanced this by benchmarking six algorithms (logistic regression [29], k-nearest neighbor [2], decision tree [133], SVM [74], RF [109], and XGBoost [57]) on multi-sequence features, highlighting SVM's discriminative edge. These efforts, however, largely centered on binary grading, leaving complex multi-class scenarios underexplored. Extending the scope, Zhang et al. [145] incorporated clinical variables, radiological semantic descriptors, and radiomic signatures to differentiate meningioma subtypes.

In parallel, multimodal MRI has proven valuable for clinical validation against standardized frameworks like the WHO classification system, which offers a surgery-oriented benchmark for grading. Jiang et al. [46] analyzed a large cohort using sequences such as T1WI, T2WI, FLAIR, DWI, and post-contrast T1, applying multivariate logistic regression to identify interpretable predictors of WHO grade and brain invasion, including indicators such as the tumor-brain interface, bone invasion, and mushroom sign that directly inform clinical decision-making. Nonetheless, manual annotation of radiological features limited quantitative depth. To refine this, Zhai et al. [142] proposed a machine learning radiomics nomogram based on multi-sequence MRI for preoperative tumor consistency classification, selecting features via variance screening and LASSO for enhanced surgical planning [128, 73, 7, 78].

The emergence of deep learning has further sophisticated multimodal integration, shifting from manual feature extraction to automated learning paradigms. Banzato et al. [6] pioneered the use of pre-trained convolutional neural networks on enhanced T1WI and apparent diffusion coefficient (ADC) images, illustrating transfer learning's potential for automated grading in smaller cohorts. For broader classification, Najjar et al. [91] designed an asymmetric 3D CNN with dual encoding paths for multi-sequence T1CE and T2-FLAIR images, facilitating Grade I/II differentiation in larger cohorts, though handcrafted designs restricted adaptability. Enhancing scalability, Kaczmarczyk et al. [52] simplified multi-sequence frameworks, and Zhang et al. [156] advanced this with a meningioma feature extraction model (MFEM) combining vision transformers and CNNs to leverage transfer learning for improved representation and cross-dataset generalization [48, 45, 68, 83].

Alternatively, segmentation-based strategies have also harnessed multimodal data for classification. Chen et al. [15] utilized attention U-Net [16] for automatic meningioma segmentation from multi-parametric MRI, followed by univariate screening and minimum redundancy maximum relevance (mRMR) feature selection to build an L1-regularized logistic regression model distinguishing high- from low-grade tumors. While effective, this hybrid setup constrained end-to-end learning. Advancing toward integration, Jun et

al. [50] introduced a two-stage model with a 3D U-Net [35] for segmentation and ResNet-based [53] classification, incorporating a correlation-weighted class activation map to boost interpretability and improve decision-making in meningioma grading [34, 70, 147, 104].

## 2.2. Unimodal-based Methods

Unimodal methods aim to classify meningiomas using a single MRI sequence. Compared to multimodal algorithms, unimodal methods offer advantages such as lower computational complexity, easier sample acquisition, and faster processing speed in resource-limited settings [75, 69, 123, 47]. Early single-sequence approaches relied on manually engineered geometric and texture features combined with classical machine learning. Czyz et al. [22] employed fractal analysis on T1WI MRI to distinguish WHO I and II meningiomas, extracting mean and maximum fractal dimensions. However, their reliance on a single feature extraction approach limited the model's ability to capture tumor complexity. To address this limitation, Hale et al. [38] employed multiple machine learning models including KNN, SVM, and ANN with hyperparameter optimization and cross-validation, demonstrating improved classification performance. It was indicated in [31] that the multi-model based method [38] relies on manually engineered features which may not fully characterize tumor morphology. Then a multiple geometric feature extraction strategy [31] was presented that combines fractal analysis with topological skeleton analysis to correlate features with pathological grading and brain tissue invasion for improving the classification performance [127, 151, 101, 71].

Radiomics-based methods have been widely applied for grading meningiomas using single-sequence MRI [148, 155, 150, 149]. Zhang et al. [157] utilized preoperative T1CE MRI to extract texture and shape features for distinguishing high- and low-grade meningiomas, demonstrating that texture-based radiomics could effectively capture tumor heterogeneity. However, their analysis was confined to single-modality features, limiting comprehensive characterization of tumor microstructure. To enrich radiomic representation, a series of studies progressively enhanced feature diversity and robustness. Chen et al. [19] introduced diffusion kurtosis imaging (DKI) based radiomics to quantify microstructural heterogeneity and identified diffusion-derived metrics (e.g., mean kurtosis and mean diffusivity) as robust discriminators of tumor grade. As pointed out in [20], the DKI based method [19] relies on diffusion-only information, restricted applicability across broader MRI protocols. Then, an automatic feature extraction strategy [20] from T1WI MRI was presented for enhancing classification robustness. In the work of [28], a radiomics scoring framework was presented that integrates both radiomic and clinical parameters to improve grading consistency and interpretability across diverse patient cohorts [154, 152, 112, 113, 95].

For detailed WHO classification, single-sequence MRI approaches have shown promise using traditional machine

**Table 1**

Multimodal-based methods.

Literatures	Data Types	# Patients	Classification Approaches	Methods
[89]	T1, T2, FLAIR, DWI, ADC	303	Grade I, grade II, grade III	Radiomics feature extraction, RF, recursive partitioning analysis
[67]	T1WI, T2WI, T1CE	90	Low-grade, high-grade	3D histogram analysis, logistic regression, ROC evaluation
[54]	T1WI, T2WI, T1CE	184	Low-grade, high-grade	Radiomics feature extraction, feature selection, SVM
[61]	T1, T2, FLAIR, DWI, ADC, T1CE	71	Grade I, grade II	Radiomics based shape and texture analysis, feature reduction, logistic regression
[26]	T1, T2, FLAIR, T1CE, DWI	124	Tumor grading	Radiomics feature extraction, SVM, RF
[60]	T1WI, T1CE, T2WI, FLAIR	1,344	Automated multi-label meningioma segmentation	Multi-sequence image preprocessing, deep learning, manual refinement, multi-compartment segmentation
[6]	PCT1W, ADC	117	Low-grade, high-grade	CNN
[39]	T1-FLAIR, T2WI, CE-T1-FLAIR	131	Low-grade, high-grade	LASSO, SVM, RF, XGBoost
[40]	T1WI, T2WI, T1C, ADC, SWI	316	Low-grade, high-grade	LASSO, RF
[46]	T1WI, T2WI, FLAIR, ADC	675	WHO grade, brain invasion	Logistic regression
[142]	T1C, T2WI, FLAIR, ADC	172	Tumor consistency	LASSO, logistic regression
[145]	T1C, T2WI	172	Tumor subtype	LASSO, logistic regression
[15]	T1WI, T2WI, T1CE	143	Low-grade, high-grade	Radiomics+machine learning
[50]	T1C, T2WI	318	Low-grade, high-grade	3D U-Net+3D ResNet; CAM interpretability
[156]	T1CE, T2-FLAIR	98	Low-grade, high-grade	CNN+vision transformer hybrid+radiomics features

learning methods. Several studies [8, 124, 62, 162] have employed handcrafted feature extraction combined with classical classifiers. For instance, tumors from T1WI MRI were segmented and their corresponding feature representations were obtained by using a pre-trained Xception network [106, 25], then RF and linear discriminant analysis (LDA) were employed for classification [80]. Decision forest models have also been introduced in which clinical, morphological, and texture features from preoperative ADC images were obtained for enhancing the performance. However, these approaches rely on manual segmentation [162] or extensive manual feature engineering [80] which limit their clinical scalability. Building on these insights, Chen et al. [14] employed systematic feature selection methods—including distance correlation [116], LASSO [118] and GBDT [32]—to refine features from contrast-enhanced T1WI MRI. The combination of LASSO based feature selection and an LDA classifier demonstrated that automated feature selection enhances interpretability and consistency in three-class meningioma classification. Despite these improvements, the fundamental limitation of handcrafted features remained: they could not fully capture the complex, hierarchical patterns inherent in medical images, motivating the shift toward deep learning approaches.

To overcome the constraints of manual feature engineering, researchers began exploring deep learning methods that could automatically learn discriminative features

from single-sequence MRI [27, 141]. In meningioma grading, most early studies employed single-modality data due to easier acquisition and standardized preprocessing [136]. Wodzinski et al. [131] classified meningiomas using pre-processed T1WI MRI that included tumor segmentation and data augmentation, applying a pre-trained 2D CNN for binary grading. However, this 2D approach could not fully capture three-dimensional tumor morphology and spatial context. To address this, Chen et al. [13] adopted a cascaded framework combining an improved U-Net for automatic segmentation and 3D convolutions for volumetric feature extraction. Using T1CE MRI with ACE sequences, their model integrated DenseNet for grading prediction, thereby enhancing spatial representation. Nevertheless, the multi-stage design increased computational cost and structural complexity. These early explorations demonstrated the potential of deep learning but also revealed the need for more streamlined and efficient architectures that could balance accuracy with computational feasibility.

Responding to the computational challenges and complexity of multi-stage pipelines, subsequent research focused on developing more elegant end-to-end architectures. Building on these advances, Yang et al. [139] proposed an end-to-end SegResNet framework that simultaneously performs tumor segmentation and automatic feature extraction from segmented regions, streamlining the workflow and improving efficiency without sacrificing high accuracy

**Table 2**

Unimodal-based methods.

Literatures	Data Types	# Patients	Classification Approaches	Methods
[22]	PCT1W	54	WHO I, WHO II	Fractal dimension analysis , logistic regression
[21]	Gadolinium-enhanced T1	175	Low-grade, high-grade	Semantic and radiomic feature analysis, RF classifier
[19]	DKI	172	Low-grade, high-grade	Whole tumor histogram analysis, multi-variate logistic regression
[20]	T1CE	98	Low-grade, high-grade	Radiomics feature extraction, LASSO selection, logistic regression
[28]	T1CE	151	Low-grade, high-grade	Radiomics+machine learning models
[31]	T1WI	107	WHO I, WHO II, WHO III	Radiomics+RF
[38]	Conventional MRI	128	WHO I,WHO II	Radiomics+ANN, SVM, logistic regression
[17]	PCT1W	1,192	Multi-grade, pathologic markers	Fine-tuned ResNet-50 deep learning model
[14]	PCT1W	150	Multi-grade classification	Radiomics texture + LASSO/LDA machine learning models
[8]	PCT1W	111	Grade I, grade II, grade III	Radiomics + SVM/RF
[13]	T1CE	113	Grade I, grade II, grade III	Radiomics + machine learning models
[80]	T1CE	113	Low-grade, high-grade	Radiomics + SVM classifier
[139]	T1CE	248	Grade I, grade II, grade III	Radiomics + machine learning models
[143]	T1CE	172	Low-grade, high-grade	Radiomics + LASSO-SVM models
[146]	T2-FLAIR	202	Soft consistency, hard consistency	Fusion of CNN and radiomics features
[161]	T1WI slices	Clinical dataset	Grade I, grade II, grade III	Improved LeNet-5 CNN with data augmentation
[124]	T1C	164	Grade I, grade II, grade III	Radiomics + ensemble machine learning models
[131]	T1WI	174	Low-grade, high-grade	2D CNN with data augmentation
[138]	T1C	131	Low-grade, high-grade	SVM

in low-grade meningiomas. Direct classification approaches without explicit segmentation have also been investigated. Yang et al. [140] proposed a deep learning radiomics model (DLRM) that extracted both radiomic and deep features from T1WI MRI using a pre-trained ResNeXt-101 network [137], and employed the light gradient boosting machine (Light-GBM) [55] algorithm to construct the classifier. However, their model required the synthetic minority over-sampling technique (SMOTE) [66] to mitigate class imbalance, indicating potential challenges in handling imbalanced clinical datasets. To enhance model robustness, Chen et al. [17] adopted a transfer learning approach based on ResNet-50 trained on postoperative T1WI MRI and validated it across internal and external cohorts. This approach demonstrated that transfer learning can effectively improve generalization across diverse patient populations without extensive data augmentation. With these architectural innovations established, researchers turned their attention to applying these advanced frameworks to increasingly complex and clinically relevant classification scenarios.

Leveraging the robust architectures developed in earlier work, recent studies have extended single-sequence approaches to tackle more challenging multi-class classification problems that better reflect clinical complexity [44, 120,

27]. Beyond binary grading, Prakash et al. [99] developed a hybrid convolutional neural network (HCNN) framework to differentiate meningioma from non-meningioma images using single-sequence T1, where key features were enhanced through ridgelet transformation and subsequently classified using CNNs architectures. Based on the classification outcomes, a segmentation algorithm was further applied to delineate tumor regions, achieving a remarkable detection accuracy of 99.81% on the BRATS 2022 dataset. While this framework demonstrated exceptional accuracy, its sole reliance on binary tumor detection limits its direct applicability to clinical grading scenarios. Addressing the clinical demand for detailed WHO three-grade classification, several studies have explored advanced architectural designs and training strategies. Zhu et al. [161] employed an improved LeNet-5 convolutional neural network for three-grade WHO classification using regional MRI images. Their framework incorporated mirroring and rotation based data augmentation, as well as over-sampling techniques to address class imbalance. However, the approach relied heavily on manual annotation and architectural tuning, which may limit adaptability across varying imaging protocols. To enhance automatic feature learning, Zhang et al. [146] trained a pyramid scene parsing network (PSPNet) [158] to automatically

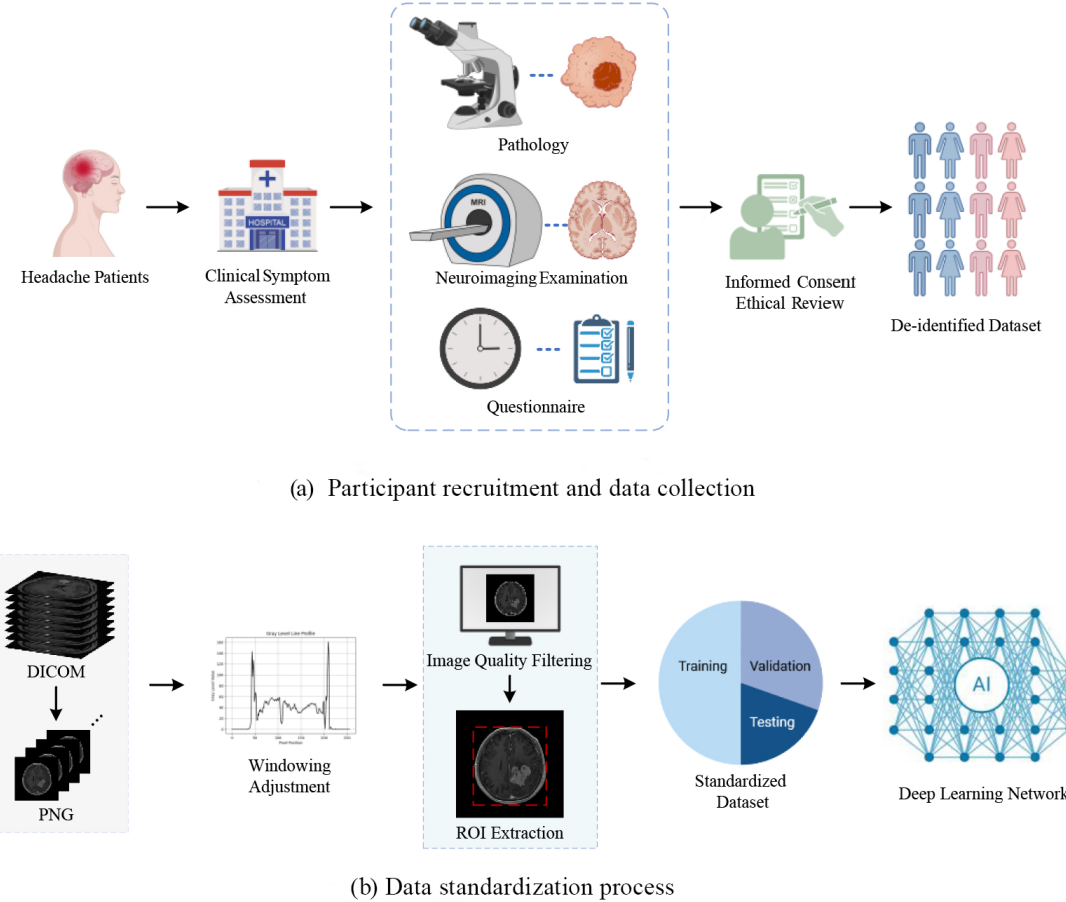


**Figure 2:** Workflow of data collection and standardization. (a) Participant recruitment and clinical data acquisition. (b) MRI data preprocessing pipeline from DICOM to standardized dataset.

detect and delineate meningiomas for three-grade classification, demonstrating that end-to-end learning can be effective in reducing dependence on manual preprocessing. While this advancement improved automation, the model primarily emphasized spatial segmentation features without adequately incorporating texture information. Recognizing that comprehensive tumor characterization requires both spatial and textural information, the same research group further proposed a dual-branch deep convolutional neural network (DB-CFCNN) [146] that integrates adaptive pooling and squeeze-and-excitation modules to capture both local spatial features and fine-grained texture representations from T2-FLAIR images. By fusing deep-learned features with radiomic descriptors through multi-classifier integration, their approach achieved enhanced robustness and performance across diverse feature domains.

### 3. Dataset and Proposed method

#### 3.1. Problem Definition

This study focuses on few-shot meningioma learning (FML). A typical few-shot learning setting [103, 153, 95, 94] consists of a support set  $\mathbf{S}$  and a query set  $\mathbf{Q}$ . The support set  $\mathbf{S}$  contains  $N$  distinct classes (corresponding to different

pathological grades or lesion types), and each class includes only  $K$  labeled samples. The query set  $\mathbf{Q}$  shares the same label space as  $\mathbf{S}$  but contains unlabeled samples. The goal of FML is to train a model that can accurately classify each query sample  $\mathbf{q}$  ( $\mathbf{q} \in \mathbf{Q}$ ) into its corresponding class using only the limited samples in the support set. Thus, the task can be formulated as an  $N$ -way  $K$ -shot meningioma learning problem.

It was indicated in [18, 1, 12, 97] that inter-class variations of medical pathology images are extremely subtle, mainly reflected in the microscopic texture distributions, nuclear morphology, and cellular structural organization. These characteristics make it challenging for the model to learn discriminative feature representations under limited data conditions [93, 41, 107]. Meanwhile, the scarcity of annotated medical data further increases the difficulty of learning transferable diagnostic representations [42, 79]. To address these challenges, we adopt an episodic training strategy, in which a large number of  $N$ -way  $K$ -shot tasks are randomly constructed from the training dataset  $\mathcal{D}_{\text{train}}$ . Each task consists of a support set and a query set, continuously simulating few-shot classification scenarios during training. This enables the model to learn discriminative and transferable feature representations for FML.

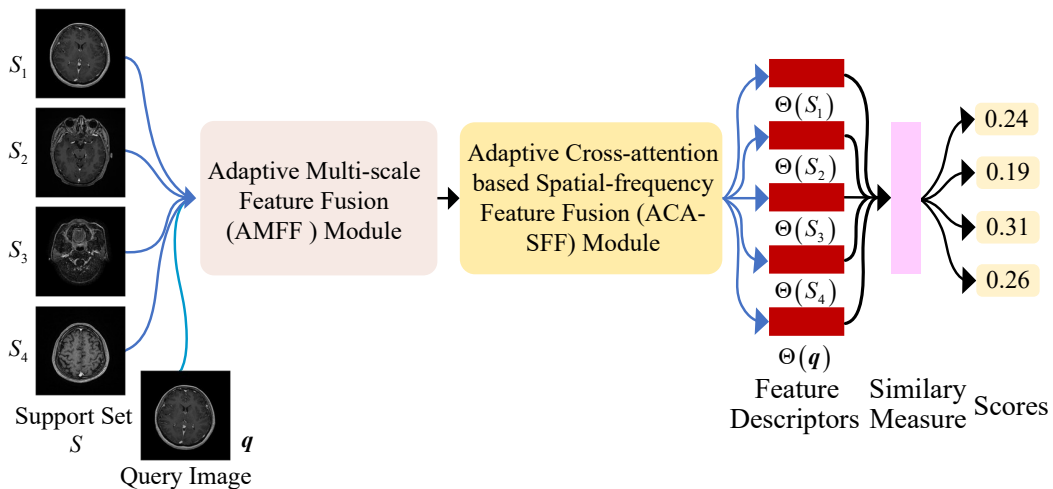


**Figure 3:** Overall architecture of the proposed adaptive multi-scale spatial-frequency network, which integrates the adaptive multi-scale feature fusion module, the adaptive cross-attention based spatial-frequency feature fusion module, the similarity module.

### 3.2. Dataset Preparation

#### 3.2.1. Data Acquisition

We developed a comprehensive dataset of meningioma patients based on data from the First Affiliated Hospital of Xi'an Jiaotong University. This dataset focuses on high-quality MRI scans to investigate the radiological features of meningiomas. All patients were diagnosed with meningioma, confirmed through clinical evaluation and histopathological examination according to the WHO classification of brain tumors. Only adult patients aged 18 years and older were included.

The dataset includes preoperative MRI scans, providing detailed anatomical information on tumor size, borders, and interactions with surrounding tissues such as edema and calcification. The high-resolution images are free from motion artifacts and other distortions, ensuring the reliability and consistency of the data for subsequent analyses.

Informed consent was obtained from all patients, and the study was approved by the Ethics Committee of the First Affiliated Hospital of Xi'an Jiaotong University, in accordance with relevant ethical guidelines. This dataset serves as a valuable resource for radiological studies of meningiomas and supports future research on tumor characterization, surgical planning, and treatment outcomes.

MRI scans were conducted for clinical purposes using a 3T Siemens Verio scanner. Acquisition parameters included the following: repetition time (RT) is set to 1,600 ms, echo time (ET) is set to 9.4 ms, inversion time (IT) is set to 708.7 ms, flip angle is set to 150°, slice thickness 1 mm, and voxel size is set to 1 mm×1 mm×1 mm. Gadolinium contrast agent was administered intravenously at 0.1 mmol/kg body weight. These imaging protocols provide high-resolution, high-contrast anatomical data for detailed assessment of tumor size, boundaries, and relationships with adjacent structures. Both preoperative and postoperative MRI scans were included, ensuring a comprehensive evaluation of tumors at

different stages of diagnosis and treatment. All imaging procedures adhered to the clinical protocols of Xi'an Jiaotong University First Affiliated Hospital.

#### 3.2.2. Ethics Statement

This study was approved by the Ethics Committee of the First Affiliated Hospital of Xi'an Jiaotong University (approval No. Menin-202401). This is a retrospective study, written informed consent for participation was not required for this study in accordance with the national legislation and the institutional requirements. All procedures involving human participants were conducted in accordance with the ethical principles of the Declaration of Helsinki.

#### 3.2.3. Data Preprocessing

We conducted comprehensive and rigorous preprocessing on 21 patient data provided by the First Affiliated Hospital of Xi'an Jiaotong University to ensure the quality of the data and the effectiveness of the training. It includes four categories: Class I (5 cases, 671 images), Class II (6 cases, 881 images), Class III (3 cases, 385 images), and Class N (7 cases without disease, 847 images). To ensure a balanced evaluation while preventing subject-level information leakage, the dataset was first partitioned at the patient level into training, validation, and testing sets with a 5:3:2 ratio. For each category, images were then uniformly sampled from the corresponding patient split for subsequent experiments.

In the data preprocessing stage, the original digital imaging and communications in medicine (DICOM) images are first converted into PNG format. While DICOM is widely used in medical imaging, it contains extensive metadata, and the PNG format eliminates this redundant information, making image processing and analysis more efficient and convenient. This conversion process ensures the integrity of the image data while maintaining consistency and operability for subsequent processing. To further enhance image quality, the DICOM images undergo intensity windowing, specifically adjusting the window width and window level to

improve contrast and reveal finer details, thereby making the images clearer. This enhancement significantly accentuates tumor regions, improving the learning effectiveness and accuracy of subsequent models. After enhancement, a preliminary screening is conducted to remove low-quality or corrupted images, ensuring that only high-quality data suitable for analysis are retained. Following this, a cropping algorithm is applied to remove the black background around the brain tissue, focusing on retaining the primary tumor region to ensure that the model training concentrates on the relevant features, thus enhancing learning outcomes and predictive performance. Finally, a custom-developed script was used to perform patient-wise dataset partitioning, ensuring that images from the same patient never appear across different splits. This patient-disjoint protocol was consistently applied throughout training, validation, and few-shot evaluation to ensure a fair and clinically meaningful assessment.

It is worth noting that, unlike natural image benchmarks where each image can be treated as an independent instance, MRI slice data exhibit strong intra-subject correlations. Therefore, during few-shot evaluation, episodic tasks were constructed under a subject-disjoint constraint, such that support and query sets never share patients from the same patient.

### 3.3. Overall Framework

As shown in Fig. 3, the proposed adaptive multi-scale spatial-frequency feature fusion network (AMSF-Net) contains two modules: an adaptive multi-scale feature fusion (AMFF) module and an adaptive cross-attention based spatial-frequency feature fusion (ACA-SFF) module. The network simultaneously leverages spatial-domain and frequency-domain representations to enhance medical image classification performance. The AMFF module captures discriminative features by performing multi-level discrete wavelet decomposition and adaptively fusing the resulting multi-scale sub-bands. The ACA-SFF module enables effective spatial-frequency fusion by establishing cross-domain interactions via an adaptive cross-attention mechanism. These fused representations are then processed by a reconstruction-based episodic classifier to yield the final results.

### 3.4. Adaptive Multi-Scale Feature Fusion (AMFF) Module

The architecture of the designed adaptive multi-scale feature fusion (AMFF) module is shown in Fig. 4(a). This module leverages hierarchical modeling and adaptive fusion to systematically extract and integrate multi-scale, multi-directional frequency information from input images, thereby delivering more discriminative frequency-aware representations for downstream networks.

For an input image  $I_0(\mathbf{n})$ , a cascaded strategy [84] is employed to perform an  $L$ -level ( $l=1, 2, \dots, L$ ) discrete wavelet transform (DWT). At the  $l$ -th ( $l=1, 2, \dots, L$ ) decomposition level, the low-frequency component from the previous level is used as the input, and one low-frequency subband together with three direction-specific high-frequency subbands are

obtained via a Haar wavelet decomposition [51], which can be formulated as below:

$$\begin{aligned} \left( I_{LL}^{(l)}(\mathbf{n}), I_{LH}^{(l)}(\mathbf{n}), I_{HL}^{(l)}(\mathbf{n}), I_{HH}^{(l)}(\mathbf{n}) \right) &= W^{(l)} \left( I_{LL}^{(l-1)}(\mathbf{n}) \right), \\ I_{LL}^{(0)}(\mathbf{n}) &= I_0(\mathbf{n}), \end{aligned} \quad (1)$$

where  $I_{LL}^{(l)}(\mathbf{n})$  denotes the low-frequency component at the  $l$ -th ( $l=1, 2, \dots, L$ ) scale.  $I_{LL}^{(l)}(\mathbf{n})$  is used to characterize the global structural information of the input image.  $I_{LH}^{(l)}(\mathbf{n})$ ,  $I_{HL}^{(l)}(\mathbf{n})$ , and  $I_{HH}^{(l)}(\mathbf{n})$  are used to characterize the high-frequency responses along the horizontal, vertical, and diagonal directions respectively, and mainly capture local textures, edges, and fine-grained variations.

Since multi-level DWT introduces downsampling operations at each decomposition stage, high-frequency subbands at different scales exhibit inconsistent spatial resolutions. To ensure that cross-scale and cross-directional features can be fused under a unified spatial coordinate system, the high-frequency subbands at each scale are reconstructed using the inverse discrete wavelet transform (IDWT), restoring them to the same spatial resolution as the input image [144, 134]. After IDWT reconstruction, the directional high-frequency responses are denoted as  $LH^{(l)}(\mathbf{n})$ ,  $HL^{(l)}(\mathbf{n})$ , and  $HH^{(l)}(\mathbf{n})$ .

Subsequently, the three reconstructed directional high-frequency subbands at the same scale are concatenated along the channel dimension to form a high-frequency representation as follows:

$$H^{(l)}(\mathbf{n}) = \text{Concat} \left( LH^{(l)}(\mathbf{n}), HL^{(l)}(\mathbf{n}), HH^{(l)}(\mathbf{n}) \right), \quad (2)$$

$$l = 1, 2, \dots, L.$$

This design explicitly preserves multi-directional frequency information while maintaining spatial consistency, thereby providing a solid foundation for subsequent direction-adaptive fusion and cross-scale modeling.

#### 3.4.1. Directional Gating

At each scale  $l$  ( $l=1, 2, \dots, L$ ), a directional gating mechanism is introduced to adaptively fuse high-frequency responses from different directions. Specifically, 2D average pooling (i.e., AvgPool2d) is first applied to the high-frequency features of the three directions for obtaining their corresponding directional statistical descriptors:

$$\begin{aligned} d_{LH}^{(l)} &= \text{AvgPool2d} \left( LH^{(l)}(\mathbf{n}) \right), \\ d_{HL}^{(l)} &= \text{AvgPool2d} \left( HL^{(l)}(\mathbf{n}) \right), \\ d_{HH}^{(l)} &= \text{AvgPool2d} \left( HH^{(l)}(\mathbf{n}) \right). \end{aligned} \quad (3)$$

Subsequently, three directional descriptors in Equation (3) are concatenated along the channel dimension and fed into a multi-layer perceptron (MLP). And a softmax normalization is then applied to obtain adaptive weights as follows:

$$\begin{aligned} [\alpha_l, \beta_l, \gamma_l] &= \text{Softmax} \left( \text{MLP} \left( d_{LH}^{(l)}, d_{HL}^{(l)}, d_{HH}^{(l)} \right) \right), \\ l &= 1, 2, \dots, L. \end{aligned} \quad (4)$$

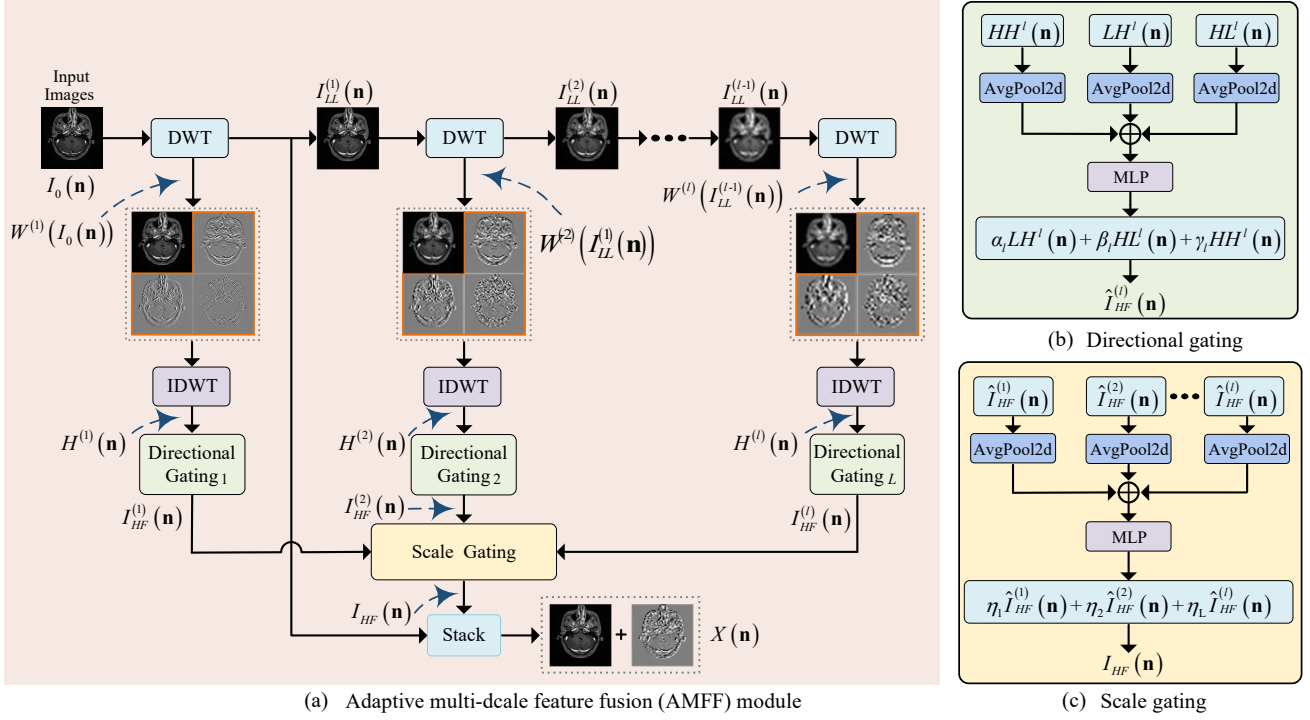


**Figure 4:** (a) Structure of the adaptive multi-scale feature feature fusion module. (b) Directional gating for adaptive fusion of  $LH$ ,  $HL$ , and  $HH$  components. (c) Scale gating for multi-scale high-frequency feature fusion.

Based on the learned directional weights, the directionally fused high-frequency representation at the  $l$ -th ( $l=1, 2, \dots, L$ ) scale is computed as:

$$\hat{I}_{HF}^{(l)}(\mathbf{n}) = \alpha_l LH^{(l)}(\mathbf{n}) + \beta_l HL^{(l)}(\mathbf{n}) + \gamma_l HH^{(l)}(\mathbf{n}). \quad (5)$$

As illustrated in Fig. 4(b), through the proposed directional gating mechanism, the model has the capability to dynamically reweight frequency responses from different directions at each scale, thereby emphasizing directionally discriminative information in the current input while suppressing redundant or noisy directional responses.

### 3.4.2. Scale Gating

As illustrated in Fig. 4(c), after completing directional fusion at each scale, a scale-gating mechanism is introduced to integrate high-frequency information across different resolution levels further. Specifically, AvgPool2d is first applied to the directionally fused high-frequency feature at each scale to obtain a scale-level descriptor:

$$s_l = \text{AvgPool2d}(\hat{I}_{HF}^{(l)}), \quad (6)$$

$$l = 1, 2, \dots, L.$$

Then, the descriptors from all scales are concatenated and fed into an MLP followed by a softmax layer to generate adaptive scale weights:

$$[\eta_1, \eta_2, \dots, \eta_L] = \text{Softmax}(\text{MLP}(s_1, s_2, \dots, s_L)), \quad (7)$$

$$l = 1, 2, \dots, L.$$

Finally, the multi-scale high-frequency fused representation is obtained by a weighted summation over the directionally fused high-frequency features at all scales:

$$I_{HF}(\mathbf{n}) = \sum_{l=1}^L \eta_l \hat{I}_{HF}^{(l)}(\mathbf{n}). \quad (8)$$

Through the proposed scale-gating mechanism, the model has the capability to adaptively select and emphasize scale-level frequency information that is more critical for the target discrimination task, according to the frequency distribution characteristics of the input sample.

At the output stage of the AMFF module, the low-frequency component obtained from the first-level decomposition, denoted as  $I_{LL}^{(1)}(\mathbf{n})$ , is preserved to maintain the global structural information and low-frequency background content of the input image. Meanwhile, the fused high-frequency feature  $I_{HF}(\mathbf{n})$  obtained through the proposed scale gating mechanism encodes fine-grained frequency characteristics across both scales and directions.

As illustrated in Fig. 4, the final output of the AMFF module is obtained by stacking the preserved low-frequency component and the fused high-frequency feature along the channel dimension:

$$X(\mathbf{n}) = \text{Stack}(I_{LL}^{(1)}(\mathbf{n}), I_{HF}(\mathbf{n})). \quad (9)$$

The resulting representation  $X(\mathbf{n})$  jointly incorporates global structural information and multi-scale frequency details, thereby providing a more discriminative input features for subsequent network modules.

Patch Embedding	Spatial Projection Head	CLS Token Insertion	Transformer Encoder
Torch.cat	Frequency Projection Head	Learnable Positional Embedding	Linear Layer
Multi-Head Attention	Positional Embedding Dropout	Layer Normalization	Softmax
Multi-layer Perceptron	Key Projection	Value Projection	Attention Weighting
Query Projection	Matrix Multiplication	Element-wise Subtraction	ReLU
	⊗	⊕	⊗
			Element-wise Product

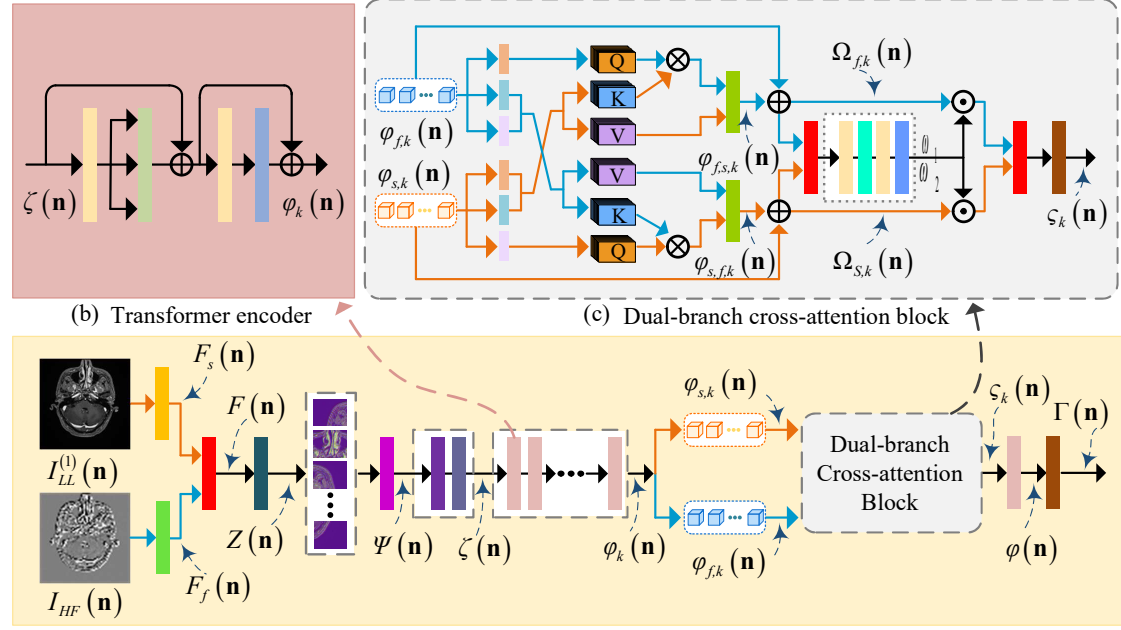


Figure 5: The architecture of the proposed ACA-SFF module which integrates dual-branch cross-attention block.

### 3.5. Adapative Cross-attention based Spatial-frequency Feature Fusion (ACA-SFF) Module

As shown in Fig. 5, an adaptive cross-attention-based spatial-frequency fusion model (ACA-SFF) is presented that leverages adaptive cross-attention to achieve bidirectional spatial-frequency interaction and adaptive region-specific fusion.

Based on the output of the AMFF module, the low-frequency component  $I_{LL}^{(1)}(\mathbf{n})$  is fused with the high-frequency component  $I_{HF}(\mathbf{n})$  as the input of the spatial and frequency domains. Firstly, the two components are fused through their respective feature maps and then projected into the unified feature space, yielding:

$$\begin{aligned} F_s(\mathbf{n}) &= P_s(I_{LL}^{(1)}(\mathbf{n})), \\ F_f(\mathbf{n}) &= P_f(I_{HF}(\mathbf{n})), \end{aligned} \quad (10)$$

where  $P_s(\cdot)$  and  $P_f(\cdot)$  represent spatial and frequency projection heads, respectively.

Later, the spatial and frequency domain features are concatenated along the channel dimension, represented as:

$$F(\mathbf{n}) = \text{Concat}(F_s(\mathbf{n}), F_f(\mathbf{n})). \quad (11)$$

After performing the patch embedding operation, the feature representation  $F(\mathbf{n})$  is partitioned into a set of non-overlapping patches and projected into a unified feature dimension, yielding a sequence of patch-level embeddings. Subsequently, a learnable CLS token (i.e.,  $Z_{cls}$ ) is prepended to the embedding sequence to form a token sequence  $\Psi(\mathbf{n})$ . On this basis, position encoding is added, and position embedding dropout is applied, resulting in the final token sequence  $\zeta(\mathbf{n})$  that is fed into the transformer encoder, defined as follows:

$$\begin{aligned} Z(\mathbf{n}) &= \text{PatchEmbed}(F(\mathbf{n})), \\ \Psi(\mathbf{n}) &= \text{Concat} [Z_{cls}, Z(\mathbf{n})], \\ \zeta(\mathbf{n}) &= \text{Dropout} (\Psi(\mathbf{n}) + E_{pos}), \end{aligned} \quad (12)$$

where  $E_{pos}$  denotes the position encoding, and  $\text{Dropout}(\cdot)$  represents the position embedding dropout operation. The resulting token sequence  $\zeta(\mathbf{n})$  is then fed into the transformer encoder for capturing global contextual relationships and producing the encoded representation  $\varphi_k(\mathbf{n})$  ( $k=1, 2, \dots, K$ ).

As shown in Fig. 5, the encoded tokens naturally preserve their domain-specific characteristics inherited from the spatial and frequency. Accordingly,  $\varphi_k(\mathbf{n})$  ( $k=1, 2, \dots, K$ ) can be regarded as consisting of spatial-domain tokens

$\varphi_{s,k}(\mathbf{n})$  and frequency-domain tokens  $\varphi_{f,k}(\mathbf{n})$ . Building upon these domain-aware token representations, the ACA-SFF module performs dual-branch cross-domain attention to facilitate explicit and bidirectional information exchange between the spatial and frequency domains.

Specifically, in the cross-domain attention between the spatial and frequency domains, the query vector  $Q_s$  is obtained from the spatial-domain token  $\varphi_{s,k}(\mathbf{n})$  ( $k=1, 2, \dots, K$ ) through linear projection, while the key and value vectors  $K_f$  and  $V_f$  are obtained from the frequency-domain token  $\varphi_{f,k}(\mathbf{n})$  through linear projection, as follows:

$$\begin{aligned} Q_s(\mathbf{n}) &= \varphi_{s,k}(\mathbf{n})W_Q^{(s)}, \\ K_f(\mathbf{n}) &= \varphi_{f,k}(\mathbf{n})W_K^{(f)}, \\ V_f(\mathbf{n}) &= \varphi_{f,k}(\mathbf{n})W_V^{(f)}, \end{aligned} \quad (13)$$

where  $W_Q^{(s)}$ ,  $W_K^{(f)}$ , and  $W_V^{(f)}$  denote learnable linear projection matrices. The corresponding spatial-to-frequency cross-domain attention output is expressed as:

$$\begin{aligned} \varphi_{s,f,k}(\mathbf{n}) &= \text{Attn}(Q_s(\mathbf{n}), K_f(\mathbf{n}), V_f(\mathbf{n})), \\ k &= 1, 2, \dots, K. \end{aligned} \quad (14)$$

Similarly, in the cross-domain attention from the frequency domain to the spatial domain, the query vector  $Q_f$  is obtained from the frequency-domain token  $\varphi_{f,k}(\mathbf{n})$  ( $k=1, 2, \dots, K$ ) through linear projection, whereas the key and value vectors  $K_s$  and  $V_s$  are obtained from the spatial-domain token  $\varphi_{s,k}(\mathbf{n})$  through linear projection, given by:

$$\begin{aligned} Q_f(\mathbf{n}) &= \varphi_{f,k}(\mathbf{n})W_Q^{(f)}, \\ K_s(\mathbf{n}) &= \varphi_{s,k}(\mathbf{n})W_K^{(s)}, \\ V_s(\mathbf{n}) &= \varphi_{s,k}(\mathbf{n})W_V^{(s)}, \\ k &= 1, 2, \dots, K. \end{aligned} \quad (15)$$

The resulting frequency-to-spatial cross-domain attention output is formulated as:

$$\begin{aligned} \varphi_{f,s,k}(\mathbf{n}) &= \text{Attn}(Q_f(\mathbf{n}), K_s(\mathbf{n}), V_s(\mathbf{n})), \\ k &= 1, 2, \dots, K. \end{aligned} \quad (16)$$

Finally, the attention operation is implemented using the scaled dot-product formulation followed by softmax normalization:

$$\text{Attn}(Q, K, V) = \text{Softmax}\left(\frac{QK^\top}{\sqrt{d}}\right)V, \quad (17)$$

where  $d$  denotes the feature dimension.

The outputs from the two cross-domain attention branches,  $\varphi_{f,s,k}(\mathbf{n})$  and  $\varphi_{s,f,k}(\mathbf{n})$ , are first combined with their corresponding input features via residual connections, resulting in the interaction-enhanced feature representations  $\Omega_{f,k}(\mathbf{n})$  and  $\Omega_{s,k}(\mathbf{n})$ , which are formulated as:

$$\begin{aligned} \Omega_{f,k}(\mathbf{n}) &= \varphi_{f,k}(\mathbf{n}) + \varphi_{s,f,k}(\mathbf{n}), \\ \Omega_{s,k}(\mathbf{n}) &= \varphi_{s,k}(\mathbf{n}) + \varphi_{f,s,k}(\mathbf{n}), \\ k &= 1, 2, \dots, K. \end{aligned} \quad (18)$$

To achieve adaptive fusion between the frequency-domain and spatial-domain features, the interaction-enhanced representations  $\Omega_{f,k}(\mathbf{n})$  and  $\Omega_{s,k}(\mathbf{n})$  are first fed into an MLP to predict the fusion weights for the two branches. The predicted weights are then normalized by a softmax function to ensure non-negativity and unit sum, yielding the weight coefficients  $\omega_1$  and  $\omega_2$  corresponding to  $\Omega_{f,k}(\mathbf{n})$  and  $\Omega_{s,k}(\mathbf{n})$ , respectively:

$$[\omega_1, \omega_2] = \text{Softmax}(\text{MLP}([\Omega_{f,k}(\mathbf{n}), \Omega_{s,k}(\mathbf{n})])), \quad (19)$$

$$k = 1, 2, \dots, K.$$

The final fused feature is obtained via a weighted summation:

$$\zeta_k(\mathbf{n}) = \omega_1 \odot \Omega_{f,k}(\mathbf{n}) + \omega_2 \odot \Omega_{s,k}(\mathbf{n}), \quad (20)$$

$$k = 1, 2, \dots, K,$$

where  $\odot$  denotes the Hadamard product.

Subsequently, the fused feature representation  $\zeta_k(\mathbf{n})$  ( $k=1, 2, \dots, K$ ) is fed into a subsequent transformer encoder for further feature modeling. The encoder output is expressed as:

$$\varphi(\mathbf{n}) = \mathcal{T}(\zeta_k(\mathbf{n})). \quad (21)$$

The output of the transformer encoder is then normalized to obtain the ACA-SFF output:

$$\Gamma(\mathbf{n}) = \text{LN}(\varphi(\mathbf{n})), \quad (22)$$

where  $\text{LN}(\cdot)$  denotes the layer normalization operation. The resulting feature representation is finally fed into task-specific prediction heads for downstream prediction.

### 3.6. Similarity Module

A reconstruction-based metric is adopted to measure the similarity between a query image and the support classes. The underlying assumption is that if a query sample belongs to a specific class, its feature representation can be well reconstructed from the support features of that class.

Let  $\mathbf{F}_q \in \mathbb{R}^{H \times W \times d}$  denote the flattened feature map of a query image, and let  $\mathcal{S}_c = \{\mathbf{S}_{c,k}\}_{k=1}^K$  denote the support set of class  $c$ . The support features are aggregated along the shot dimension to obtain a class-level support feature representation:

$$\bar{\mathbf{S}}_c = \frac{1}{K} \sum_{k=1}^K \mathbf{S}_{c,k}, \quad \bar{\mathbf{S}}_c \in \mathbb{R}^{H \times W \times d}. \quad (23)$$

Both the flattened feature map of the query image  $\mathbf{F}_q$  and the class-level support feature representation  $\bar{\mathbf{S}}_c$  are normalized using  $\ell_2$  normalization along the channel dimension.

The similarity computation is formulated as a feature reconstruction problem. In few-shot learning scenarios, the feature dimension  $d$  (e.g., 640) is typically much larger than the spatial resolution  $r = H \times W$  (e.g., 196). Therefore, instead of explicitly constructing a projection operator, the

reconstruction problem is solved in the feature space following the dual ridge regression formulation proposed in FRN [130]. By applying the Woodbury matrix identity, the optimal closed-form reconstruction matrix is obtained as:

$$\hat{\mathbf{W}}_c = (\tilde{\mathbf{S}}_c^\top \tilde{\mathbf{S}}_c + \lambda \mathbf{E}_d)^{-1} \tilde{\mathbf{S}}_c^\top \tilde{\mathbf{S}}_c, \quad (24)$$

$$\lambda = \text{Softplus}(\alpha) \cdot \gamma + \epsilon.$$

where  $\mathbf{E}_d \in \mathbb{R}^{d \times d}$  denotes the identity matrix,  $\alpha$  is a learnable parameter used to control the regularization strength, and  $\gamma$  and  $\epsilon$  are scaling and smoothing constants, respectively. The Softplus( $\cdot$ ) function is adopted to ensure the non-negativity of the regularization coefficient  $\lambda$ , thereby avoiding numerical instability. In implementation,  $\gamma$  is set to 10 and  $\epsilon$  is set to 0.01. This adaptive formulation allows the model to automatically adjust the degree of shrinkage during training.

The reconstructed query features with respect to class  $c$  are then obtained using the reconstruction matrix:

$$\tilde{\mathbf{F}}_c = \mathbf{F}_q \hat{\mathbf{W}}_c. \quad (25)$$

To further refine the reconstruction and compensate for potential feature misalignment, a learnable scalar parameter  $\beta$  is introduced to compute a calibration factor, and the calibrated reconstruction is obtained as:

$$\hat{\mathbf{F}}_c = \rho \cdot \tilde{\mathbf{F}}_c, \quad (26)$$

$$\rho = 1 + \text{Sigmoid}(\beta).$$

where  $\hat{\mathbf{F}}_c$  denotes the reconstructed query features before calibration.

Finally, the similarity between the query image and class  $c$  is measured by the reconstruction quality of the query features with respect to the class-specific support subspace. Specifically, we compute the mean squared reconstruction error between each spatial token of the query feature map and its corresponding reconstructed feature, and average the errors over all spatial locations. Since a smaller reconstruction error indicates that the query sample is more consistent with the class, we take the negative mean reconstruction error as the similarity score:

$$\text{score}_c = -\frac{1}{H \times W} \sum_{i=1}^{H \times W} \left\| \mathbf{f}_{q,i} - \hat{\mathbf{f}}_{c,i} \right\|_2^2, \quad (27)$$

where  $\mathbf{f}_{q,i}$  denotes the  $i$ -th spatial token of the query feature map  $\mathbf{F}_q$ , and  $\hat{\mathbf{f}}_{c,i}$  denotes the corresponding reconstructed token from  $\hat{\mathbf{F}}_c$ , obtained using the support features of class  $c$ .

The predicted probability of the query sample belonging to class  $c$  is computed using a softmax function with a learnable temperature parameter  $\tau$ :

$$P(y = c \mid \mathbf{F}_q) = \frac{\exp(\tau \cdot \text{score}_c)}{\sum_j \exp(\tau \cdot \text{score}_j)}. \quad (28)$$

**Table 3**

Sample distribution for each class and dataset.

Dataset	Class	Train	Val	Test	Total
COVID	COVID	2,531	543	542	3,616
	Lung_opacity	4,208	902	902	6,012
	Normal	7,134	1,529	1,529	10,192
	Viral pneumonia	942	201	202	1,345
XJTU Meningioma	No_tumor	192	78	115	385
	WHO_1	168	102	115	385
	WHO_2	190	90	105	385
	WHO_3	192	78	115	385
Brain Tumor MRI	Glioma	810	486	324	1,620
	Meningioma	817	491	327	1,635
	Notumor	865	519	347	1,731
	Pituitary	870	522	348	1,740

During training, the temperature parameter  $\tau$  is implemented as a learnable scaling factor, initialized as  $\tau=15.0$ , and constrained within  $[0.1, 100]$  to ensure stable optimization.

## 4. Experiments

### 4.1. Datasets

The proposed AMSF-Net is evaluated on three medical imaging datasets: XJTU Meningioma, Brain Tumor MRI, and COVID [86, 10]. Each dataset contains four classes, with the COVID dataset split by 70%, 15% and 15%, and both the Brain Tumor MRI and XJTU Meningioma datasets split by 50%, 30% and 20% into training, validation, and test sets, respectively. The detailed class-wise sample distribution is summarized in Table 3.

### 4.2. Implementation Details

ViT-B/16 with ImageNet-21k pre-training [117] is adopted as the backbone for feature extraction. All experiments are conducted using the PyTorch framework on a single NVIDIA RTX 3090 GPU. The initial learning rate is set to  $2 \times 10^{-5}$  with a weight decay of  $5 \times 10^{-5}$ . The model is trained for 8,000 epochs with the learning rate decreased by a factor of 0.5 at epochs  $\{1, 500, 2, 500, 3, 500, 4, 500, 5, 500\}$ , and validation conducted every 500 epochs. A 300-epoch warm-up strategy is applied to stabilize training. Random cropping, horizontal flipping, rotation ( $\pm 10^\circ$ ), and DWT transformation are applied for data augmentation. For all experiments, this paper validates the average accuracy of 10,000 randomly generated tasks on the test dataset under the standard 4-way 1-shot and 4-way 5-shot settings with a 95% confidence interval.

### 4.3. Performance Comparison

In this part, we first compare the proposed AMSF-Net model with four state-of-the-art methods. The baseline methods mainly adopt ResNet-12 [30] or Conv-4 [93] as backbones; meanwhile, we additionally report the results of Proto-Net with a ViT-Base backbone as a reference under a

**Table 4**

Performance comparison on different datasets.

Train shot	Method	Backbone	XJTU Meningioma		Brain Tumor MRI		COVID	
			1-shot	5-shot	1-shot	5-shot	1-shot	5-shot
1-shot	Proto-Net [114]	ResNet-12	97.79 $\pm$ 0.04	98.25 $\pm$ 0.03	97.52 $\pm$ 0.08	98.14 $\pm$ 0.03	89.69 $\pm$ 0.17	92.81 $\pm$ 0.06
	FRN [130]	ResNet-12	97.35 $\pm$ 0.06	97.86 $\pm$ 0.03	97.32 $\pm$ 0.08	98.09 $\pm$ 0.03	90.26 $\pm$ 0.16	92.86 $\pm$ 0.06
	C2-Net [85]	ResNet-12	97.70 $\pm$ 0.06	98.64 $\pm$ 0.06	78.18 $\pm$ 0.57	81.69 $\pm$ 0.31	91.10 $\pm$ 0.34	93.40 $\pm$ 0.13
	Bi-FRN [132]	ResNet-12	98.50 $\pm$ 0.08	97.67 $\pm$ 0.04	97.57 $\pm$ 0.06	97.99 $\pm$ 0.03	90.56 $\pm$ 0.08	92.87 $\pm$ 0.14
	Proto-Net [114]	Conv-4	86.95 $\pm$ 0.14	94.30 $\pm$ 0.06	88.34 $\pm$ 0.15	92.73 $\pm$ 0.06	77.37 $\pm$ 0.21	85.86 $\pm$ 0.09
	FRN [130]	Conv-4	78.92 $\pm$ 0.20	85.22 $\pm$ 0.09	86.05 $\pm$ 0.18	90.75 $\pm$ 0.07	73.92 $\pm$ 0.23	82.47 $\pm$ 0.09
	C2-Net [85]	Conv-4	96.65 $\pm$ 0.23	97.46 $\pm$ 0.08	97.26 $\pm$ 0.15	97.98 $\pm$ 0.07	89.53 $\pm$ 0.37	92.23 $\pm$ 0.14
	Bi-FRN [132]	Conv-4	96.83 $\pm$ 0.08	96.27 $\pm$ 0.05	97.05 $\pm$ 0.07	97.70 $\pm$ 0.04	89.84 $\pm$ 0.17	92.42 $\pm$ 0.07
	Proto-Net [114]	ViT-Base	98.17 $\pm$ 0.36	98.67 $\pm$ 0.23	95.98 $\pm$ 0.90	96.57 $\pm$ 0.41	91.90 $\pm$ 1.13	93.97 $\pm$ 0.59
	<b>AMSF-Net (Ours)</b>	ViT-Base	<b>99.70<math>\pm</math>0.01</b>	<b>99.72<math>\pm</math>0.01</b>	<b>99.19<math>\pm</math>0.02</b>	<b>99.33<math>\pm</math>0.02</b>	<b>92.51<math>\pm</math>0.15</b>	<b>94.42<math>\pm</math>0.06</b>
5-shot	Proto-Net [114]	ResNet-12	99.21 $\pm$ 0.02	99.49 $\pm$ 0.03	97.57 $\pm$ 0.07	98.01 $\pm$ 0.03	92.31 $\pm$ 0.14	94.47 $\pm$ 0.06
	FRN [130]	ResNet-12	99.06 $\pm$ 0.02	99.33 $\pm$ 0.03	97.08 $\pm$ 0.08	97.60 $\pm$ 0.03	91.51 $\pm$ 0.14	93.36 $\pm$ 0.06
	C2-Net [85]	ResNet-12	94.89 $\pm$ 0.34	98.06 $\pm$ 0.08	97.42 $\pm$ 0.17	98.10 $\pm$ 0.07	91.56 $\pm$ 0.34	93.81 $\pm$ 0.13
	Bi-FRN [132]	ResNet-12	98.47 $\pm$ 0.06	99.24 $\pm$ 0.02	97.99 $\pm$ 0.06	98.33 $\pm$ 0.03	92.31 $\pm$ 0.14	94.91 $\pm$ 0.05
	Proto-Net [114]	Conv-4	94.64 $\pm$ 0.09	98.43 $\pm$ 0.03	89.61 $\pm$ 0.14	95.72 $\pm$ 0.05	81.29 $\pm$ 0.10	89.45 $\pm$ 0.08
	FRN [130]	Conv-4	95.07 $\pm$ 0.11	98.43 $\pm$ 0.03	92.47 $\pm$ 0.13	96.46 $\pm$ 0.05	83.52 $\pm$ 0.19	90.02 $\pm$ 0.07
	C2-Net [85]	Conv-4	93.48 $\pm$ 0.38	98.05 $\pm$ 0.07	97.56 $\pm$ 0.13	98.13 $\pm$ 0.07	89.33 $\pm$ 0.36	93.23 $\pm$ 0.14
	Bi-FRN [132]	Conv-4	96.85 $\pm$ 0.09	98.70 $\pm$ 0.03	96.68 $\pm$ 0.07	97.69 $\pm$ 0.04	88.90 $\pm$ 0.16	93.54 $\pm$ 0.06
	Proto-Net [114]	ViT-Base	97.87 $\pm$ 0.45	99.00 $\pm$ 0.25	95.52 $\pm$ 1.14	97.40 $\pm$ 0.39	88.47 $\pm$ 1.07	93.85 $\pm$ 0.59
	<b>AMSF-Net (Ours)</b>	ViT-Base	<b>99.76<math>\pm</math>0.02</b>	<b>99.79<math>\pm</math>0.02</b>	<b>99.32<math>\pm</math>0.02</b>	<b>99.51<math>\pm</math>0.02</b>	<b>93.47<math>\pm</math>0.14</b>	<b>95.58<math>\pm</math>0.02</b>

transformer-backbone setting. ViT-B/16 is employed as the backbone to investigate transformer-based architectures for few-shot medical image analysis. The experiments encompass the XJTU Meningioma, Brain Tumor MRI, and COVID datasets, with detailed results presented in Table 3.

As shown in Table 4, the proposed method consistently outperforms existing approaches on the XJTU Meningioma dataset. For instance, on our newly constructed XJTU Meningioma dataset, the proposed approach achieves superior results in both 4-way 1-shot and 4-way 5-shot classification tasks, thereby validating the efficacy of AMSF-Net. Specifically, in the 4-way 1-shot setting, AMSF-Net yields accuracy improvements of 12.75%, 20.78%, 3.05%, 2.87%, 1.91%, 2.35%, 2%, and 1.2% relative to Proto-Net [114], FRN [130], C2-Net [85], and Bi-FRN [132] (with Conv-4 backbone) and the corresponding methods (with ResNet-12 backbone), respectively. In the 4-way 5-shot setting, the respective gains are 5.12%, 4.69%, 6.28%, 2.91%, 0.55%, 0.7%, 4.87%, and 1.29%.

To further verify the effectiveness of the proposed method, we perform t-SNE visualizations comparing AMSF-Net with the ResNet-12-based FRN [130] on the Brain Tumor MRI dataset under the 4-way 1-shot and 4-way 5-shot settings. As shown in Fig. 6, AMSF-Net generates more uniformly distributed and well-separated feature embeddings, demonstrating enhanced class separability.

Additionally, we perform a comparative analysis of AMSF-Net against mainstream benchmarks on the Brain Tumor MRI dataset. The findings demonstrate that AMSF-Net attains higher accuracy across all categories, particularly

in challenging differentiation tasks, exhibiting superior discriminative power and underscoring the model's robustness in tumor subtype classification.

Additionally, as illustrated in Fig. 7, the confusion matrices on the Brain Tumor MRI dataset further validate the superiority of AMSF-Net. Compared with the ResNet-12-based FRN [130], AMSF-Net exhibits clearer diagonal dominance and fewer off-diagonal errors under both 4-way 1-shot and 4-way 5-shot settings, indicating more accurate and stable predictions across tumor subtypes. These results demonstrate that the proposed method achieves better inter-class separability and stronger robustness in challenging tumor differentiation tasks.

#### 4.4. Ablation Study

To isolate the contribution of each proposed component, we conduct an ablation study on the Brain Tumor MRI dataset under a fixed ViT-B/16 backbone with ImageNet-21k pretraining. All ablation experiments follow the same training configuration, data augmentation strategy, and evaluation protocol as described in the experimental settings.

Importantly, subject-wise data splits and subject-disjoint episodic sampling are strictly enforced throughout all experiments to ensure that no patient appears in both support and query sets, thereby preventing patient-level information leakage.

**Table 5**

Ablation study on Brain Tumor MRI under the same ViT-B/16 backbone.

Method (ViT-B/16)	AMFF	ACA-SFF	1-shot	5-shot
ViT baseline	✗	✗	95.12±0.03	96.22±0.01
ViT + AMFF	✓	✗	96.34±0.04	97.11±0.03
ViT + ACA-SFF	✗	✓	96.77±0.02	97.58±0.02
AMSF-Net (Ours)	✓	✓	<b>99.32±0.02</b>	<b>99.51±0.02</b>

**Table 6**

Ablation study on ACA-SFF insertion depth across different datasets.

Insertion Stage	Layer Index	XJTU Meningioma		Brain Tumor MRI		COVID	
		1-shot	5-shot	1-shot	5-shot	1-shot	5-shot
Early Fusion	3	98.67	98.93	98.52	98.72	92.31	94.01
Middle Fusion	6	98.88	98.97	98.65	98.83	92.48	94.51
Deep Fusion	9	98.31	98.48	98.14	98.64	91.53	93.88
Ours	11	<b>99.76</b>	<b>99.79</b>	<b>99.32</b>	<b>99.51</b>	<b>93.47</b>	<b>95.58</b>

#### 4.4.1. The Impact of AMFF and ACA-SFF on Performance

We conduct an ablation study to investigate the contribution of each proposed component, including the AMFF module and the ACA-SFF module.

As summarized in Table 5, introducing AMFF into the vanilla ViT baseline leads to a noticeable performance improvement. Specifically, the 1-shot accuracy increases from 95.12% to 96.34%, while the 5-shot accuracy improves from 96.22% to 97.11%. This result highlights the effectiveness of explicitly modeling multi-scale frequency-domain information.

Building upon AMFF, the inclusion of the ACA-SFF module further boosts performance by enabling bidirectional interactions between spatial and frequency representations. With ACA-SFF, the model achieves 96.77% accuracy in the 1-shot setting and 97.58% in the 5-shot setting.

When both modules are jointly integrated, the complete AMSF-Net delivers the best performance across all evaluation settings, reaching 99.32% accuracy for 1-shot classification and 99.51% for 5-shot classification. Notably, the combined improvement consistently surpasses that obtained by either module alone, indicating a strong complementarity between AMFF and ACA-SFF. While AMFF enriches

multi-scale frequency representations, ACA-SFF adaptively fuses spatial and frequency features through cross-attention.

Overall, the ablation results demonstrate that the performance gains are not solely attributable to the ViT backbone or large-scale pretraining, but arise from the proposed spatial-frequency fusion mechanisms.

#### 4.4.2. The Impact of ACA-SFF Insertion Layer

We study the effect of ACA-SFF insertion depth by placing it at different backbone stages while keeping all other settings unchanged. As shown in Table 6, we compare early fusion (layer index 3), middle fusion (layer index 6), and deep fusion (layer index 9). The results indicate that the insertion depth noticeably affects few-shot performance across datasets. In particular, inserting ACA-SFF at a deeper layer achieves the best overall performance, and thus, we adopt layer index 11 as the default setting in subsequent experiments.

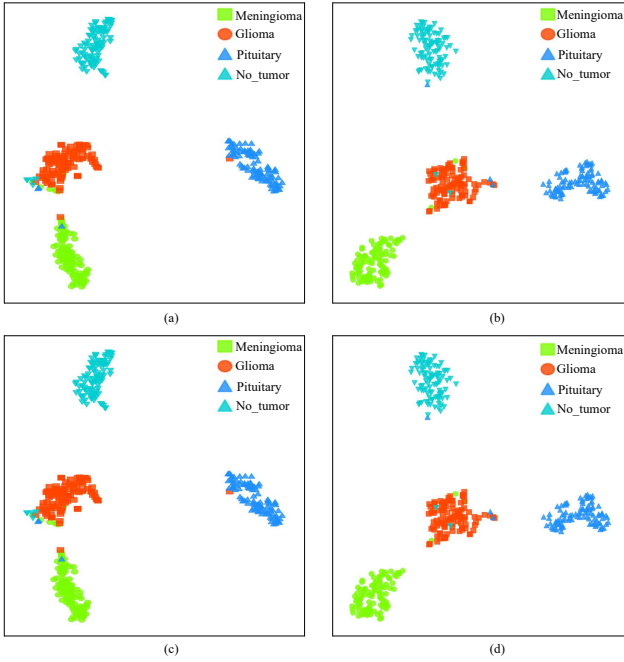
#### 4.4.3. The Impact of DWT Decomposition Level

Table 7 presents an ablation study on the number of DWT decomposition levels  $L$ . As  $L$  increases from 1 to 3, the classification performance consistently improves across all datasets and both 1-shot and 5-shot settings, indicating that multi-scale frequency representations are beneficial for

**Table 7**

Ablation study on DWT decomposition level. Results are reported as mean±std over 3 runs. Best results are in bold.

Model	Backbone	XJTU Meningioma		Brain Tumor MRI		COVID	
		1-shot	5-shot	1-shot	5-shot	1-shot	5-shot
AMSF-Net (Ours) (DWT level=1)	ViT	99.32±0.02	99.35±0.02	98.82±0.04	98.96±0.03	92.81±0.14	94.89±0.05
AMSF-Net (Ours) (DWT level=2)	ViT	99.46±0.01	99.47±0.01	99.02±0.04	99.26±0.02	93.02±0.14	94.93±0.05
AMSF-Net (Ours) (DWT level=3)	ViT	<b>99.76±0.02</b>	<b>99.79±0.02</b>	<b>99.32±0.02</b>	<b>99.51±0.02</b>	<b>93.47±0.14</b>	<b>95.58±0.02</b>
AMSF-Net (Ours) (DWT level=4)	ViT	99.55±0.02	99.56±0.02	99.14±0.02	99.27±0.02	93.08±0.13	95.04±0.03



**Figure 6:** t-SNE visualization of feature distributions on the Brain Tumor MRI dataset. Subplots (a) and (b) show the feature representations learned by FRN [130] under 4-way 1-shot and 4-way 5-shot tasks, respectively; (c) and (d) show the results obtained by AMSF-Net under 4-way 1-shot and 4-way 5-shot settings, respectively.

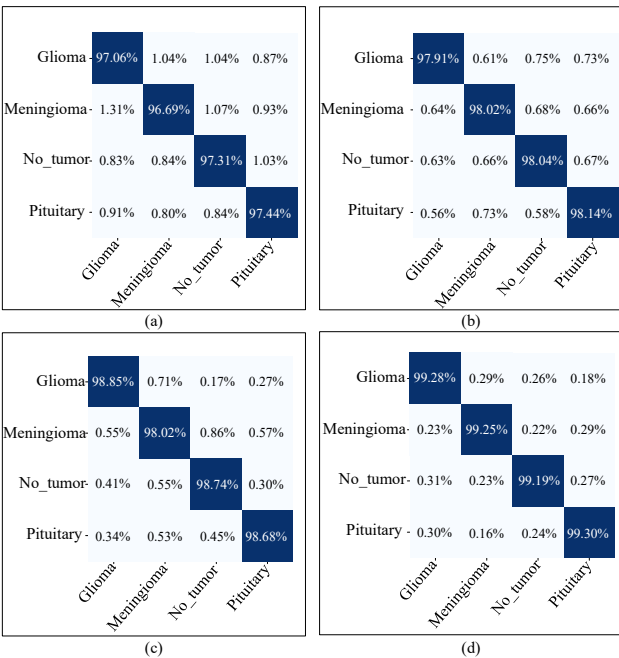


**Figure 7:** Confusion matrices on the Brain Tumor MRI dataset. (a) and (b) show the results of FRN [130] under the 4-way 1-shot and 4-way 5-shot settings, respectively; (c) and (d) show the results of AMSF-Net under the 4-way 1-shot and 4-way 5-shot settings, respectively. Each row represents the true class and each column represents the predicted class.

few-shot medical image classification. Shallow decomposition ( $L=1$ ) captures limited frequency information and fails to adequately model fine-grained texture patterns, while moderate depths ( $L=2, 3$ ) effectively balance global structural cues and localized high-frequency details. However, further increasing the decomposition depth to  $L=4$  leads to performance saturation or slight degradation, which can be attributed to excessive frequency fragmentation, noise amplification, and information loss introduced by repeated downsampling and reconstruction. Overall,  $L=3$  achieves the best trade-off between representation richness and robustness, and is therefore adopted as the default setting.

## 5. Conclusion

This study proposes an innovative AMSF-Net framework, which achieves significant advancements in the challenging task of meningioma grading and classification under limited annotated data. By explicitly integrating spatial and frequency domain features and leveraging a domain-aware transformer architecture, the proposed approach substantially enhances the model's feature representation and discriminative ability in few-shot learning scenarios. An adaptive fusion mechanism further strengthens the extraction of critical imaging features, enabling the model to consistently outperform existing state-of-the-art methods in meningioma classification tasks. Extensive experiments conducted on both our self-constructed and soon-to-be-released XJTU meningioma dataset, as well as other public benchmark datasets, comprehensively validate the effectiveness and robustness of the proposed method. These findings demonstrate its considerable potential and academic value for intelligent diagnosis of meningioma.

## References

- Abel, J., Jain, S., Rajan, D., et al., 2024. AI powered quantification of nuclear morphology in cancers enables prediction of genome instability and prognosis. *NPJ Precision Oncology* 8, 134.
- Al-Zaiti, S.S., Martin-Gill, C., Zègre-Hemsey, J.K., et al., 2023. Machine learning for ECG diagnosis and risk stratification of occlusion myocardial infarction. *Nature Medicine* 29, 1804–1813.
- An, Y., Jing, J., Zhang, W., 2023. Edge detection using multi-directional anisotropic gaussian directional derivative. *Signal, Image and Video Processing* 17, 3767–3774.
- Azad, R., Kazerouni, A., Heidari, M., et al., 2024a. Advances in medical image analysis with vision Transformers: A comprehensive review. *Medical Image Analysis* 91, 103000.
- Azad, R., Kazerouni, A., Heidari, M., et al., 2024b. Advances in medical image analysis with vision transformers: A comprehensive review. *Medical Image Analysis* 91, 103000.
- Banzato, T., Causin, F., Della Puppa, A., et al., 2019. Accuracy of deep learning to differentiate the histopathological grading of meningiomas on MR images: A preliminary study. *Journal of Magnetic Resonance Imaging* 50, 1152–1159.
- Bao, J., Jing, J., Zhang, W., Liu, C., Gao, T., 2022. A corner detection method based on adaptive multi-directional anisotropic diffusion. *Multimedia Tools and Applications* 81, 28729–28754.
- Bayley, J.C., Mergenthaler, S., Daggubati, V., et al., 2022. Multiple approaches converge on three biological subtypes of meningioma. *Science Advances* 8, eabm6247.

[9] Beque, M.P.L., Lobbes, M.B.I., van Wijk, Y., et al., 2023. Combining deep learning and handcrafted radiomics for classification of suspicious lesions on contrast-enhanced mammograms. *Radiology* 307, e221843.

[10] Bougourzi, F., Distante, C., Dornaika, F., et al., 2023. PDAtt-UNet: Pyramid dual-decoder attention UNet for COVID-19 infection segmentation from CT-scans. *Medical Image Analysis* 86, 102797.

[11] Brady, A.P., Allen, B., Chong, J., et al., 2024. Developing, purchasing, implementing and monitoring AI tools in radiology: Practical considerations. A multi-society statement from the ACR, CAR, ESR, RANZCR and RSNA. *Radiology: Artificial Intelligence* 6, e230513.

[12] Brussee, S., Buzzanca, G., Schrader, A.M.R., et al., 2025. Graph neural networks in histopathology: Emerging trends and future directions. *Medical Image Analysis* 101, 103444.

[13] Chen, C., Cheng, Y., Xu, J., et al., 2021. Automatic meningioma segmentation and grading prediction: A hybrid deep-learning method. *Journal of Personalized Medicine* 11, 786.

[14] Chen, C., Guo, X., Wang, J., et al., 2019. The diagnostic value of radiomics-based machine learning in predicting the grade of meningiomas using conventional magnetic resonance imaging: A preliminary study. *Frontiers in Oncology* 9, 1338.

[15] Chen, H., Li, S., Zhang, Y., et al., 2022a. Deep learning-based automatic segmentation of meningioma from multiparametric MRI for preoperative meningioma differentiation using radiomic features: A multicentre study. *European Radiology* 32, 7248–7259.

[16] Chen, H., Li, S., Zhang, Y., et al., 2022b. Deep learning-based automatic segmentation of meningioma from multiparametric MRI for preoperative meningioma differentiation using radiomic features: A multicentre study. *European Radiology* 32, 7248–7259.

[17] Chen, J., Xue, Y., Ren, L., et al., 2024a. Predicting meningioma grades and pathologic marker expression via deep learning. *European Radiology* 34, 2997–3008.

[18] Chen, R.J., Ding, T., Lu, M.Y., et al., 2024b. Towards a general-purpose foundation model for computational pathology. *Nature Medicine* 30, 850–862.

[19] Chen, X., Lin, L., Wu, J., et al., 2020. Histogram analysis in predicting the grade and histological subtype of meningiomas based on diffusion kurtosis imaging. *Acta Radiologica* 61, 1228–1239.

[20] Chu, H., Lin, X., He, J., et al., 2021. Value of MRI radiomics based on enhanced T1WI images in prediction of meningiomas grade. *Academic Radiology* 28, 687–693.

[21] Coroller, T.P., Bi, W.L., Huynh, E., et al., 2017. Radiographic prediction of meningioma grade by semantic and radiomic features. *PLoS One* 12, e0187908.

[22] Czyz, M., Radwan, H., Li, J.Y., et al., 2017. Fractal analysis may improve the preoperative identification of atypical meningiomas. *Neurosurgery* 80, 300–308.

[23] Dembrower, K., Crippa, A., Colón, E., et al., 2023. Artificial intelligence for breast cancer detection in screening mammography in Sweden: A prospective, population-based, paired-reader, non-inferiority study. *The Lancet Digital Health* 5, e703–e711.

[24] Derry, A., Krzywinski, M., Altman, N., 2023. Convolutional neural networks. *Nature Methods* 20, 1269–1270.

[25] Disci, R., Gurcan, F., Soylu, A., 2025. Advanced brain tumor classification in MR images using transfer learning and pre-trained deep CNN models. *Cancers* 17, 121.

[26] Dorfner, F.J., Patel, J.B., Kalpathy-Cramer, J., et al., 2025a. A review of deep learning for brain tumor analysis in MRI. *NPJ Precision Oncology* 9, 2.

[27] Dorfner, F.J., Patel, J.B., Kalpathy-Cramer, J., et al., 2025b. A review of deep learning for brain tumor analysis in MRI. *NPJ Precision Oncology* 9, 2.

[28] Duan, C., Zhou, X., Wang, J., et al., 2022. A radiomics nomogram for predicting the meningioma grade based on enhanced T1WI images. *The British Journal of Radiology* 95, 20220141.

[29] Durmaz, E.S., Karabacak, M., Ozkara, B.B., et al., 2023. Radiomics-based machine learning models in STEMI: A promising tool for the prediction of major adverse cardiac events. *European Radiology* 33, 4611–4620.

[30] Feng, J., Zhang, H., Wang, Z., 2025. Eternal-MAML: A meta-learning framework for cross-domain defect recognition. *Peer Computer Science* 11, e2757.

[31] Frisonnet, G., Baudouin, M., Brinjikji, W., et al., 2022. Advanced MRI shape analysis as a predictor of histologically aggressive supratentorial meningioma. *Journal of Neuroradiology* 49, 275–280.

[32] Friedman, J.H., 2001. Greedy function approximation: A gradient boosting machine. *Annals of Statistics* 29, 1189–1232.

[33] Gao, S., Li, Z.Y., Han, Q., et al., 2023. RF-Next: Efficient receptive field search for convolutional neural networks. *IEEE Transactions on Pattern Analysis and Machine Intelligence* 45, 2984–3002.

[34] Gao, T., Jing, J., Liu, C., Zhang, W., Gao, Y., Sun, C., 2020. Fast corner detection using approximate form of second-order gaussian directional derivative. *IEEE Access* 8, 194092–194104.

[35] Gi, Y., Oh, G., Jo, Y., et al., 2024. Study of multistep dense U-Net-based automatic segmentation for head MRI scans. *Medical Physics* 51, 2230–2238.

[36] Groff, K.J., Patel, R.V., Feng, Y., et al., 2025. The effect of TERT promoter mutation on predicting meningioma outcomes: A multi-institutional cohort analysis. *The Lancet Oncology* 26, 1178–1190.

[37] Gui, C., Wang, J.Z., Patil, V., et al., 2025. Analysis of TERT association with clinical outcome in meningiomas: A multi-institutional cohort study. *The Lancet Oncology* 26, 1191–1203.

[38] Hale, A.T., Stonko, D.P., Wang, L., et al., 2018. Machine learning analyses can differentiate meningioma grade by features on magnetic resonance imaging. *Neurosurgical Focus* 45, E4.

[39] Han, Y., Wang, T., Wu, P., et al., 2021. Meningiomas: Preoperative predictive histopathological grading based on radiomics of MRI. *Magnetic Resonance Imaging* 77, 36–43.

[40] Hu, J., Zhao, Y., Li, M., et al., 2020. Machine learning-based radiomics analysis in predicting the meningioma grade using multiparametric MRI. *European Journal of Radiology* 131, 109251.

[41] Huang, S.C., Pareek, A., Jensen, M., et al., 2023a. Self-supervised learning for medical image classification: A systematic review and implementation guidelines. *NPJ Digital Medicine* 6, 74.

[42] Huang, S.C., Pareek, A., Jensen, M., et al., 2023b. Self-supervised learning for medical image classification: A systematic review and implementation guidelines. *NPJ Digital Medicine* 6, 74.

[43] Hwang, K.P., Elshafeey, N.A., Kotrotsou, A., et al., 2023. A radiomics model based on synthetic MRI acquisition for predicting neoadjuvant systemic treatment response in triple-negative breast cancer. *Radiology: Imaging Cancer* 5, e230009.

[44] Ilani, M.A., Shi, D., Banad, Y.M., 2025. T1-weighted MRI-based brain tumor classification using hybrid deep learning models. *Scientific Reports* 15, 7010.

[45] Islam, M.A., Zhou, J., Zhang, W., Gao, Y., 2023. Background-aware band selection for object tracking in hyperspectral videos. *IEEE Geoscience and Remote Sensing Letters* 20, 1–5.

[46] Jiang, J., Yu, J., Liu, X., et al., 2022. The efficacy of preoperative mri features in the diagnosis of meningioma WHO grade and brain invasion. *Frontiers in Oncology* 12, 1100350.

[47] Jing, J., Liu, C., Zhang, W., Gao, Y., Sun, C., 2023. Ecfnet: Effective corner feature representations network for image corner detection. *Expert Systems with Applications* 211, 118673.

[48] Jing, J., Liu, S., Liu, C., Gao, T., Zhang, W., Sun, C., 2021. A novel decision mechanism for image edge detection, in: *International Conference on Intelligent Computing*, Springer. pp. 274–287.

[49] Jing, J., Liu, S., Wang, G., Zhang, W., Sun, C., 2022. Recent advances on image edge detection: A comprehensive review. *Neurocomputing* 503, 259–271.

[50] Jun, Y., Park, Y.W., Shin, H., et al., 2023. Intelligent noninvasive meningioma grading with a fully automatic segmentation using interpretable multiparametric deep learning. *European Radiology* 33, 6124–6133.

[51] K A, N., M N, A.K., 2026. Haar-initialized parametric wavelet compression with attention-driven lightweight CNN for brain tumor

classification on edge devices. *Biomedical Physics & Engineering Express* 12.

[52] Kaczmarczyk, R., et al., 2024. Evaluating multimodal AI in medical diagnostics. *NPJ Digital Medicine* 7, 125.

[53] Kang, Z., Xiao, E., Li, Z., et al., 2024. Deep learning based on ResNet-18 for classification of prostate imaging-reporting and data system category 3 lesions. *Academic Radiology* 31, 2412–2423.

[54] Ke, C., Chen, H., Lv, X., et al., 2020. Differentiation between benign and nonbenign meningiomas by using texture analysis from multiparametric MRI. *Journal of Magnetic Resonance Imaging* 51, 1810–1820.

[55] Ke, G., Meng, Q., Finley, T., et al., 2017. LightGBM: A highly efficient gradient boosting decision tree, in: *Advances in Neural Information Processing Systems*.

[56] Kelly, B.S., Quinn, C., Belton, N., et al., 2023. Cybersecurity considerations for radiology departments involved with artificial intelligence. *European Radiology* 33, 8833–8841.

[57] Klontzas, M.E., Leventis, D., Spanakis, K., et al., 2023. Post-mortem CT radiomics for the prediction of time since death. *European Radiology* 33, 8387–8395.

[58] LaBella, D., Khanna, O., McBurney-Lin, S., et al., 2024a. A multi-institutional meningioma MRI dataset for automated multi-sequence image segmentation. *Scientific Data* 11, 496.

[59] LaBella, D., Khanna, O., McBurney-Lin, S., et al., 2024b. A multi-institutional meningioma MRI dataset for automated multi-sequence image segmentation. *Scientific Data* 11, 496.

[60] LaBella, D., Khanna, O., McBurney-Lin, S., et al., 2024c. A multi-institutional meningioma MRI dataset for automated multi-sequence image segmentation. *Scientific Data* 11, 496.

[61] Laukamp, K.R., Shakirin, G., Baeßler, B., et al., 2019. Accuracy of radiomics-based feature analysis on multiparametric magnetic resonance images for noninvasive meningioma grading. *World Neurosurgery* 132, e366–e390.

[62] Lee, J.Y., Kim, J., Lee, D.H., et al., 2025. Single-cell analysis reveals a longitudinal trajectory of meningioma evolution and heterogeneity. *Nature Communications* 16.

[63] Lei, T., Song, W., Zhang, W., Du, X., Li, C., He, L., Nandi, A.K., 2024. Semi-supervised 3-d medical image segmentation using multiconsistency learning with fuzzy perception-guided target selection. *IEEE Transactions on Radiation and Plasma Medical Sciences* 9, 421–432.

[64] Li, J., Chen, J., Tang, Y., et al., 2023a. Transforming medical imaging with transformers? A comparative review of key properties, current progresses, and future perspectives. *Medical Image Analysis* 85, 102762.

[65] Li, J., Chen, J., Tang, Y., et al., 2023b. Transforming medical imaging with transformers? A comparative review of key properties, current progresses, and future perspectives. *Medical Image Analysis* 85, 102762.

[66] Li, X., Huang, X., Shen, Y., et al., 2025. Machine learning for grading prediction and survival analysis in high grade glioma. *Scientific Reports* 15, 16955.

[67] Li, X., Miao, Y., Han, L., et al., 2019a. Meningioma grading using conventional MRI histogram analysis based on 3D tumor measurement. *European Journal of Radiology* 110, 45–53.

[68] Li, Y., Bi, Y., Zhang, W., Ren, J., Chen, J., 2023c. M 2gf: Multi-scale and multi-directional gabor filters for image edge detection. *Applied Sciences* 13, 9409.

[69] Li, Y., Bi, Y., Zhang, W., Sun, C., 2019b. Multi-scale anisotropic gaussian kernels for image edge detection. *IEEE Access* 8, 1803–1812.

[70] Li, Y., Feng, B., Zhang, W., 2023d. Mutual interference mitigation of millimeter-wave radar based on variational mode decomposition and signal reconstruction. *Remote Sensing* 15, 557.

[71] Li, Y., Zhang, W., 2023. Traffic flow digital twin generation for highway scenario based on radar-camera paired fusion. *Scientific reports* 13, 642.

[72] Liao, Y., Gao, Y., Zhang, W., 2025. Dynamic accumulated attention map for interpreting evolution of decision-making in vision transformer. *Pattern Recognition* 165, 111607.

[73] Liao, Y., Zhang, W., Gao, Y., Sun, C., Yu, X., 2022. Asrsnet: Automatic salient region selection network for few-shot fine-grained image classification, in: *International Conference on Pattern Recognition and Artificial Intelligence*, Springer, pp. 627–638.

[74] Lin, R.Y., Zheng, Y.N., Lv, F.J., et al., 2023. A combined non-enhanced CT radiomics and clinical variable machine learning model for differentiating benign and malignant sub-centimeter pulmonary solid nodules. *Medical Physics* 50, 2835–2843.

[75] Liu, T., Xu, J., Lei, T., Wang, Y., Du, X., Zhang, W., Lv, Z., Gong, M., 2024. Aekan: Exploring superpixel-based autoencoder kolmogorov-arnold network for unsupervised multimodal change detection. *IEEE Transactions on Geoscience and Remote Sensing* .

[76] Liu, W., Liu, T., Han, T., et al., 2023. Multi-modal deep-fusion network for meningioma presurgical grading with integrative imaging and clinical data. *The Visual Computer* 39, 3561–3571.

[77] Lu, J., Peng, G., Zhang, W., Sun, C., 2023. Track-before-detect algorithm based on cost-reference particle filter bank for weak target detection. *IEEE Access* 11, 121688–121701.

[78] Lu, J., Zhang, W., Zhao, Y., Sun, C., 2022. Image local structure information learning for fine-grained visual classification. *Scientific Reports* 12, 19205.

[79] Lu, M.Y., Chen, B., Williamson, D.F.K., et al., 2024. A visual-language foundation model for computational pathology. *Nature Medicine* 30, 863–874.

[80] Lu, Y., Liu, L., Luan, S., et al., 2019. The diagnostic value of texture analysis in predicting WHO grades of meningiomas based on adc maps: An attempt using decision tree and decision forest. *European Radiology* 29, 1318–1328.

[81] Lucas, C.G., Mirchia, K., Seo, K., et al., 2024. Spatial genomic, biochemical and cellular mechanisms underlying meningioma heterogeneity and evolution. *Nature Genetics* 56, 1121–1133.

[82] Luo, Z., Zhou, L., Bai, X., et al., 2020. Aslfeat: Learning local features of accurate shape and localization, in: *Proceedings of the IEEE Conference on Computer Vision and Pattern Recognition*, pp. 6589–6598.

[83] Ma, B., Guo, J., Zhai, T.T., van der Schaaf, A., Steenbakkers, R.J., van Dijk, L.V., Both, S., Langendijk, J.A., Zhang, W., Qiu, B., et al., 2023. Ct-based deep multi-label learning prediction model for outcome in patients with oropharyngeal squamous cell carcinoma. *Medical Physics* 50, 6190–6200.

[84] Ma, Z., Chen, Z., Zhao, L., et al., 2024a. Cross-layer and cross-sample feature optimization network for few-shot fine-grained image classification, in: *Proceedings of the AAAI Conference on Artificial Intelligence*, pp. 5668–5676.

[85] Ma, Z., Chen, Z., Zhao, L., et al., 2024b. Cross-layer and cross-sample feature optimization network for few-shot fine-grained image classification, in: *Proceedings of the AAAI Conference on Artificial Intelligence*, pp. 5668–5676.

[86] Mahmoud, E., Gass, J., Dhemesh, Y., et al., 2025. MU-Glioma Post: A comprehensive dataset of automated MR multi-sequence segmentation and clinical features. *Scientific Data* 12, 1847.

[87] Maniar, K.M., Lassarén, P., Rana, A., et al., 2023. Traditional machine learning methods versus deep learning for meningioma classification, grading, outcome prediction, and segmentation: A systematic review and meta-analysis. *World Neurosurgery* 179, e119–e134.

[88] Miao, L., Jiang, J., Li, J., et al., 2025. Whole-tumor histogram analysis of synthetic MRI for the differentiation of benign and malignant soft-tissue tumors: A preliminary study. *European Radiology* 35, 7888–7899.

[89] Morin, O., Chen, W.C., Nassiri, F., et al., 2019. Integrated models incorporating radiologic and radiomic features predict meningioma grade, local failure, and overall survival. *Neuro-oncology Advances* 1, vdz011.

[90] Pahud de Mortanges, A., Luo, H., Shu, S.Z., et al., 2024. Orchestrating explainable artificial intelligence for multimodal and longitudinal data in medical imaging. *NPJ Digital Medicine* 7, 195.

[91] Najjar, R., et al., 2023. Redefining radiology: AI and ML in radiology. *Insights into Imaging* 14, 118.

[92] Pachetti, E., Colantonio, S., 2024a. A systematic review of few-shot learning in medical imaging. *Artificial Intelligence in Medicine* 156, 102949.

[93] Pachetti, E., Colantonio, S., 2024b. A systematic review of few-shot learning in medical imaging. *Artificial Intelligence in Medicine* 156, 102949.

[94] Pan, Z., Yu, X., Zhang, M., Zhang, W., Gao, Y., 2024a. DyCR: A dynamic clustering and recovering network for few-shot class-incremental learning. *IEEE transactions on Neural Networks and Learning Systems* 36, 7116–7129.

[95] Pan, Z., Zhang, W., Yu, X., Zhang, M., Gao, Y., 2024b. Pseudo-set frequency refinement architecture for fine-grained few-shot class-incremental learning. *Pattern Recognition* 155, 110686.

[96] Patel, R.V., Yao, S., Huang, R.Y., et al., 2023. Application of radiomics to meningiomas: A systematic review. *Neuro-Oncology* 25, 1166–1176.

[97] Paverd, H., Zormpas-Petridis, K., Clayton, H., et al., 2024. Radiology and multi-scale data integration for precision oncology. *NPJ Precision Oncology* 8, 158.

[98] Piffer, S., Ubaldi, L., Tangaro, S., et al., 2024. Tackling the small data problem in medical image classification with artificial intelligence: A systematic review. *Progress in Biomedical Engineering* 6.

[99] Prakash, B.V., Kannan, A.R., Santhiyakumari, N., et al., 2023. Meningioma brain tumor detection and classification using hybrid cnn method and ridgelet transform. *Scientific Reports* 13, 14522.

[100] Price, M., Ballard, C., Benedetti, J., et al., 2024. Cbtrus statistical report: Primary brain and other central nervous system tumors diagnosed in the united states in 2017–2021. *Neuro-Oncology* 26, vi1–vi185.

[101] Qiu, B., Guo, J., Kraeima, J., Glas, H.H., Zhang, W., Borra, R.J., Witjes, M.J.H., van Ooijen, P.M., 2021. Recurrent convolutional neural networks for 3d mandible segmentation in computed tomography. *Journal of personalized medicine* 11, 492.

[102] Ren, J., An, Y., Lei, T., Yang, J., Zhang, W., Pan, Z., Liao, Y., Gao, Y., Sun, C., Zhang, W., 2025. Adaptive feature selection-based feature reconstruction network for few-shot learning. *Pattern Recognition* .

[103] Ren, J., An, Y., Lei, T., Yang, J., Zhang, W., Pan, Z., Liao, Y., Gao, Y., Sun, C., Zhang, W., 2026. Adaptive feature selection-based feature reconstruction network for few-shot learning. *Pattern Recognition* , 112289.

[104] Ren, J., Li, C., An, Y., Zhang, W., Sun, C., 2024. Few-shot fine-grained image classification: A comprehensive review. *AI* 5, 405–425.

[105] Sahm, F., Bertero, L., Brandner, S., et al., 2025. European association of neuro-oncology guideline on molecular testing of meningiomas for targeted therapy selection. *Neuro-Oncology* 27, 869–883.

[106] Sathya, R., Mahesh, T.R., Bhatia Khan, S., et al., 2024. Employing Xception convolutional neural network through high-precision MRI analysis for brain tumor diagnosis. *Frontiers in Medicine* 11, 1487713.

[107] Schäfer, R., Nicke, T., Höfener, H., et al., 2024. Overcoming data scarcity in biomedical imaging with a foundational multi-task model. *Nature Computational Science* 4, 495–509.

[108] Schouten, D., Nicoletti, G., Dille, B., et al., 2025. Navigating the landscape of multimodal AI in medicine: A scoping review on technical challenges and clinical applications. *Medical Image Analysis* 105, 103621.

[109] Shahabi, F., Battalio, S.L., Pfammatter, A.F., et al., 2024. A machine-learned model for predicting weight loss success using weight change features early in treatment. *NPJ Digital Medicine* 7, 344.

[110] Shamshad, F., Khan, S., Zamir, S.W., et al., 2023a. Transformers in medical imaging: A survey. *Medical Image Analysis* 88, 102802.

[111] Shamshad, F., Khan, S., Zamir, S.W., et al., 2023b. Transformers in medical imaging: A survey. *Medical Image Analysis* 88, 102802.

[112] Shui, P.L., Zhang, W.C., 2012. Noise-robust edge detector combining isotropic and anisotropic gaussian kernels. *Pattern Recognition* 45, 806–820.

[113] Shui, P.L., Zhang, W.C., 2013. Corner detection and classification using anisotropic directional derivative representations. *IEEE Transactions on Image Processing* 22, 3204–3218. doi:10.1109/TIP.2013.2259834.

[114] Snell, J., Swersky, K., Zemel, R., 2017. Prototypical networks for few-shot learning, in: *Advances in Neural Information Processing Systems*, pp. 4077–4087.

[115] Soni, N., Ora, M., Bathla, G., et al., 2025. Meningioma: Molecular updates from the 2021 world health organization classification of CNS tumors and imaging correlates. *American Journal of Neuroradiology* 46, 240–250.

[116] Székely, G.J., Rizzo, M.L., Bakirov, N.K., 2007. Measuring and testing dependence by correlation of distances. *Annals of Statistics* 35, 2769–2794.

[117] Tayebi Arasteh, S., Misra, L., Kather, J.N., et al., 2024. Enhancing diagnostic deep learning via self-supervised pretraining on large-scale, unlabeled non-medical images. *European Radiology Experience* 8, 10.

[118] Tibshirani, R., 1996. Regression shrinkage and selection via the LASSO. *Journal of the Royal Statistical Society: Series B* 58, 267–288.

[119] Upreti, T., Dube, S., Pareek, V., et al., 2024. Meningioma grading via diagnostic imaging: A systematic review and meta-analysis. *Neuroradiology* 66, 1301–1310.

[120] van der Voort, S.R., Incekara, F., Wijnenga, M.M.J., et al., 2023. Combined molecular subtyping, grading, and segmentation of glioma using multi-task deep learning. *Neuro-Oncology* 25, 279–289.

[121] Wach, J., Basaran, A.E., Arlt, F., et al., 2023. Cdkn2a/b deletions are strongly associated with meningioma progression: A meta-analysis of individual patient data. *Acta Neuropathologica Communications* 11, 189.

[122] Wang, J., Lu, J., Yang, J., Wang, M., Zhang, W., 2024a. An unbiased feature estimation network for few-shot fine-grained image classification. *Sensors* 24, 7737.

[123] Wang, J., Zhang, W., 2018. A survey of corner detection methods, in: *2018 2nd International Conference on Electrical Engineering and Automation (ICEEA 2018)*, Atlantis Press. pp. 214–219.

[124] Wang, J.Z., Bohman, L.E., Raleigh, D.R., et al., 2024b. Molecular classification to refine surgical and radiation decision-making in meningioma. *Nature Medicine* 30, 2706–2716.

[125] Wang, J.Z., Landry, A.P., Raleigh, D.R., et al., 2024c. Meningioma: International consortium on meningiomas consensus review on scientific advances and treatment paradigms for clinicians, researchers, and patients. *Neuro-Oncology* 26, 1742–1780.

[126] Wang, J.Z., Patil, V., Landry, A.P., et al., 2024d. Molecular classification to refine surgical and radiotherapeutic decision-making in meningioma. *Nature Medicine* 30, 3173–3183.

[127] Wang, M., Zhang, W., Sun, C., et al., 2020. Corner detection based on shearlet transform and multi-directional structure tensor. *Pattern Recognition* 103, 107299.

[128] Wang, M., Zheng, B., Wang, G., Yang, J., Lu, J., Zhang, W., 2025. A principal component analysis-based feature optimization network for few-shot fine-grained image classification. *Mathematics* 13, 1098.

[129] Weller, M., Wen, P.Y., Chang, S.M., et al., 2024. Glioma. *Nature Reviews Disease Primers* 10, 33.

[130] Wertheimer, D., Tang, L., Hariharan, B., 2021. Few-shot classification with feature map reconstruction networks, in: *Proceedings of the IEEE Conference on Computer Vision and Pattern Recognition*, pp. 8012–8021.

[131] Wodzinski, M., Banzato, T., Atzori, M., et al., 2020. Training deep neural networks for small and highly heterogeneous MRI datasets for cancer grading, in: *Machine Learning in Medical Imaging*, pp.

1758–1761.

[132] Wu, J., Chang, D., Sain, A., et al., 2023a. Bi-directional feature reconstruction network for fine-grained few-shot image classification, in: Proceedings of the AAAI Conference on Artificial Intelligence, pp. 3367–3375.

[133] Wu, T., Wei, Y., Wu, J., et al., 2023b. Logistic regression technique is comparable to complex machine learning algorithms in predicting cognitive impairment related to post intensive care syndrome. *Scientific Reports* 13, 2485.

[134] Wu, W., Wang, Y., Liu, Q., et al., 2024. Wavelet-improved score-based generative model for medical imaging. *IEEE Transactions on Medical Imaging* 43, 966–979.

[135] Xiao, S., Zeng, S., Kou, Y., 2025a. MRI radiomics in diagnosing high and low grade meningiomas through systematic review and meta analysis. *Scientific Reports* 15, 17521.

[136] Xiao, S., Zeng, S., Kou, Y., 2025b. MRI radiomics in diagnosing high and low grade meningiomas through systematic review and meta analysis. *Scientific Reports* 15, 17521.

[137] Xie, S., Girshick, R., Dollar, P., et al., 2017. Aggregated residual transformations for deep neural networks, in: Proceedings of the IEEE Conference on Computer Vision and Pattern Recognition.

[138] Yan, P.F., Yan, L., Hu, T.T., et al., 2017. The potential value of preoperative MRI texture and shape analysis in grading meningiomas: A preliminary investigation. *Translational Oncology* 10, 570–577.

[139] Yang, L., Wang, T., Zhang, J., et al., 2024. Deep learning-based automatic segmentation of meningioma from T1-weighted contrast-enhanced MRI for preoperative meningioma differentiation using radiomic features. *BMC Medical Imaging* 24, 56.

[140] Yang, L., Xu, P., Zhang, Y., et al., 2022. A deep learning radiomics model may help to improve the prediction performance of preoperative grading in meningioma. *Neuroradiology* 64, 1373–1382.

[141] Yang, Y., Guo, X., Ye, C., et al., 2023. CReg-KD: Model refinement via confidence regularized knowledge distillation for brain imaging. *Medical Image Analysis* 89, 102916.

[142] Zhai, Y., Song, D., Yang, F., et al., 2021. Preoperative prediction of meningioma consistency via machine learning-based radiomics. *Frontiers in Oncology* 11, 657288.

[143] Zhang, H., Mo, J., Jiang, H., et al., 2021a. Deep learning model for the automated detection and histopathological prediction of meningioma. *Neuroinformatics* 19, 393–402.

[144] Zhang, J., Mao, H., Chang, D., et al., 2024a. Adaptive and iterative learning with multi-perspective regularizations for metal artifact reduction. *IEEE Transactions on Medical Imaging* 43, 3354–3365.

[145] Zhang, J., Zhang, G., Cao, Y., et al., 2022. A magnetic resonance imaging-based radiomic model for the noninvasive preoperative differentiation between transitional and atypical meningiomas. *Frontiers in Oncology* 12, 811767.

[146] Zhang, J., Zhao, Y., Lu, Y., et al., 2024b. Meningioma consistency assessment based on the fusion of deep learning features and radiomics features. *European Journal of Radiology* 170, 111343.

[147] Zhang, W., Liu, X., Xue, Z., Gao, Y., Sun, C., 2021b. Ndpnet: A novel non-linear data projection network for few-shot fine-grained image classification. *arXiv preprint arXiv:2106.06988* .

[148] Zhang, W., Sun, C., 2019. Corner detection using second-order generalized gaussian directional derivative representations. *IEEE transactions on pattern analysis and machine intelligence* 43, 1213–1224.

[149] Zhang, W., Sun, C., 2020. Corner detection using multi-directional structure tensor with multiple scales. *International Journal of Computer Vision* 128, 438–459.

[150] Zhang, W., Sun, C., Breckon, T., et al., 2019. Discrete curvature representations for noise robust image corner detection. *IEEE Transactions on Image Processing* 28, 4444–4459.

[151] Zhang, W., Sun, C., Gao, Y., 2023. Image intensity variation information for interest point detection. *IEEE Transactions on Pattern Analysis and Machine Intelligence* 45, 9883–9894.

[152] Zhang, W., Zhao, Y., Breckon, T.P., Chen, L., 2017. Noise robust image edge detection based upon the automatic anisotropic gaussian kernels. *Pattern Recognition* 63, 193–205.

[153] Zhang, W., Zhao, Y., Gao, Y., Sun, C., 2024c. Re-abstraction and perturbing support pair network for few-shot fine-grained image classification. *Pattern Recognition* 148, 110158.

[154] Zhang, W.C., Shui, P.L., 2015. Contour-based corner detection via angle difference of principal directions of anisotropic gaussian directional derivatives. *Pattern Recognition* 48, 2785–2797.

[155] Zhang, W.C., Wang, F.P., Zhu, L., et al., 2014. Corner detection using Gabor filters. *IET Image Processing* 8, 639–646.

[156] Zhang, Z., Miao, Y., Wu, J., et al., 2024d. Deep learning and radiomics-based approach to meningioma grading: Exploring the potential value of peritumoral edema regions. *Physics in Medicine and Biology* 69.

[157] Zhang, Z., Yao, J., Wu, X., et al., 2024e. Deep learning and radiomics-based approach to meningioma grading: Exploring the value of peritumoral edema. *Physics in Medicine & Biology* 69, 105002.

[158] Zhao, H., Shi, J., Qi, X., et al., 2017. Pyramid scene parsing network, in: Proceedings of the IEEE Conference on Computer Vision and Pattern Recognition.

[159] Zhao, Z., Nie, C., Zhao, L., et al., 2024. Multi-parametric MRI-based machine learning model for prediction of WHO grading in patients with meningiomas. *European Radiology* 34, 2468–2479.

[160] Zheng, Z., Ren, H., Wu, Y., Zhang, W., Lu, H., Yang, Y., Shen, H.T., 2023. Fully unsupervised domain-agnostic image retrieval. *IEEE Transactions on Circuits and Systems for Video Technology* 34, 5077–5090.

[161] Zhu, H., Fang, Q., He, H., et al., 2019a. Automatic prediction of meningioma grade image based on data amplification and improved convolutional neural network. *Computational and Mathematical Methods in Medicine* 2019, 7289273.

[162] Zhu, Y., Man, C., Gong, L., et al., 2019b. A deep learning radiomics model for preoperative grading in meningioma. *European Journal of Radiology* 116, 128–134.